

Impacts of background wind on the interactions between urban breeze circulation and convective cells: Ensemble large-eddy simulations

Seong-Ho Hong¹ | Han-Gyul Jin² | Jong-Jin Baik¹

¹School of Earth and Environmental Sciences, Seoul National University, Seoul, South Korea

²Department of Atmospheric Sciences, Pusan National University, Busan, South Korea

Correspondence

Jong-Jin Baik, School of Earth and Environmental Sciences, Seoul National University, Seoul 08826, South Korea.
 Email: jbaik@snu.ac.kr

Funding information

National Research Foundation of Korea, Grant/Award Number:
 2021R1A2C1007044

Abstract

Urban breeze is produced by the temperature difference between urban and surrounding rural areas, and its interactions with other atmospheric phenomena are of great interest. In this study, the impacts of background wind on the interactions between urban breeze circulation (UBC) and convective cells are numerically investigated. For this, a large number of idealized ensemble simulations are performed using the Weather Research and Forecasting-large-eddy simulation model, where the initial background wind speed varies from 0 to $5 \text{ m}\cdot\text{s}^{-1}$ in $0.5 \text{ m}\cdot\text{s}^{-1}$ intervals. As the background wind speed increases, the location of the strongest updraft moves from the urban center to the downwind boundary of the urban area. This is associated with different interactions between the UBC and convective cells under different background wind speeds. For no background wind, the UBC is relatively strong and its center is located at the urban center, producing a strong updraft there. Convective cells are advected toward the UBC center and merge with the strong updraft, further intensifying it. For weak background wind, the UBC is relatively weak and its center is located near the downwind urban boundary. Convective cells passing the urban area merge with each other and intensify, and after they pass the downwind urban boundary, the strong vertical wind shear in the right part of the UBC tilts and weakens them. For strong background wind, the UBC is very weak and convective cells are advected mainly by the strong background wind. These changes in the characteristics of convective cells in and around the urban area with background wind speed may lead to the changes in the preferred location of cloud initiation and cloud development.

KEY WORDS

background wind, cell merging and tilting, convective cells, large-eddy simulation, urban breeze circulation

1 | INTRODUCTION

Cities induce or modify local winds and weather (Cotton & Pielke, 1995). One of the most extensively studied urban-related phenomena is the urban heat island (UHI), that is, an urban area having higher near-surface temperature than its surrounding rural areas. The UHI in the daytime is mainly caused by a larger surface sensible heat flux in the urban area than in the rural areas. The difference in the surface sensible heat flux generally originates from the difference in moisture availability between urban and rural surfaces (Christen & Vogt, 2004; Oke, 1982). The daytime UHI intensity has been observed to be about 0.5–3°C in warm seasons (Borbora & Das, 2014; Lee & Baik, 2010; Zhang et al., 2021). The UHI produces pressure anomalies that can induce a mesoscale circulation in the lower troposphere called the urban breeze (UB) circulation (UBC) or the UHI circulation. Many observational (e.g., Fujibe & Asai, 1980; Hidalgo et al., 2008b; Wong & Dirks, 1978), laboratory-experimental (e.g., Cenedese & Monti, 2003; Falasca et al., 2013), and numerical modeling (e.g., Ganbat et al., 2015; Hidalgo et al., 2008a; Lemonsu & Masson, 2002; Wang, 2009; Wang & Li, 2016) studies have been conducted to better understand the UBC. The UBC is pronounced on days with clear skies and calm conditions (Oke et al., 2017). The UBC in these conditions exhibits inward flows (from the rural areas to the urban center) in the lower part, strong upward motions at the urban center, outward flows in the upper part, and weak downward motions in the surrounding rural areas.

The convective boundary layer in warm seasons frequently exhibits organized shallow convection such as cellular convection and convective rolls (Banghoff et al., 2020) (hereafter collectively called convective cells). A convective cell is comprised of updraft and downdraft parts. Its characteristics depend on surface sensible heat flux and vertical wind shear (Atkinson & Zhang, 1996; Khanna & Brasseur, 1998; Moeng & Sullivan, 1994; Salesky et al., 2017).

Convective cells can interact with mesoscale circulations such as sea breeze circulation and dryline circulation. Through an idealized numerical simulation of a sea breeze and convective cells in a dry condition, Ogawa et al. (2003) found that the sea breeze frontal updraft intensifies when it merges with updrafts of convective cells. Jiang et al. (2017) examined the interactions between a sea breeze front and turbulent flows using idealized numerical simulations over an urban-like building array in a dry condition. They showed that the sea breeze frontal updraft is enhanced when it merges with updrafts of turbulent structures that are in intermediate modes between cellular convection and convective rolls. Using idealized numerical simulations, Peckham et al. (2004) investigated

the interactions between a dryline and convective cells. They showed that the dryline updraft is locally enhanced at its intersections with updrafts of convective cells and a deep convective cloud is initiated at one of the intersections. Xue and Martin (2006) performed numerical simulations of a real case observed during the 2002 International H₂O Project to examine the role of the interactions between a dryline and convective rolls in the initiation of intense moist convection. They showed that at the dryline convergence boundary, the interactions produce surface convergence maxima which cause strong updrafts and trigger moist convection. These studies indicate that the interactions of a mesoscale circulation with convective cells can impact the updraft intensity of the mesoscale circulation.

Convective cells also appear over urban areas, which has been detected in observational studies (Kropfli & Kohn, 1978; Miao & Chen, 2008), and the UBC can interact with them. Miao and Chen (2008) observed cloud streets from satellite images, which are a manifestation of the presence of convective rolls, in the southwestern part of Beijing, China. Chen et al. (2015) simulated convective rolls over Sendai Airport and its surrounding areas and reported that convective rolls originating from major built-up areas have stronger updrafts than those originating from rice paddy fields. Ryu et al. (2013) examined the interaction of the UBC with convective cells in a calm and effectively dry (i.e., no clouds) condition using a numerical simulation. In their simulation, an UB front is formed and advances toward the urban center. As the UB front advances, it merges with convective cells in the urban area and also with convective cells advected from the surrounding rural area by the UB, intensifying the updraft of the UB front.

Although Ryu et al. (2013) clearly showed how the UBC interacts with convective cells, the simulation was conducted in a calm condition (no background wind). To examine the interactions in more realistic conditions, background wind should be considered in the simulation. However, how the UBC interacts with convective cells in the presence of background wind has not been investigated yet. Because it has been revealed by many previous studies that the characteristics of the UBC (e.g., location, intensity, and associated updraft features) change with background wind speed (e.g., Han & Baik, 2008; Lemonsu & Masson, 2002; Martilli, 2002; Omidvar et al., 2020; Wang et al., 2019; Wang et al., 2020; Zhang et al., 2014), its interactions with convective cells are expected to be also significantly affected by background wind. This investigation could be valuable for understanding convective activities in cities and their surrounding areas under different background wind conditions. Though this study focuses on convection under an effectively dry

condition, its conclusions are expected to provide some insights into the relationship between background wind and urban-induced moist convection, which leads to the downwind enhancement of precipitation (Han et al., 2014; Qian et al., 2022).

In this study, we examine the impacts of background wind on the UBC-convective cell interactions through simulations with different background wind speeds in an effectively dry condition, extending the work of Ryu et al. (2013). In Section 2, the experimental set-up is described. The results and discussion are given in Section 3. A summary and conclusions are provided in Section 4.

2 | EXPERIMENTAL SET-UP

This study uses the Weather Research and Forecasting (WRF) model version 4.1.3 (Skamarock et al., 2019). The physics parametrization options used for simulations are the Dudhia short-wave radiation scheme (Dudhia, 1989), the rapid radiative transfer model long-wave radiation scheme (Mlawer et al., 1997), the unified Noah land surface model (Tewari et al., 2004), the revised MM5 surface layer scheme (Jiménez et al., 2012), and the WRF double-moment 6-class microphysics scheme (Lim & Hong, 2010). Instead of a planetary boundary layer (PBL) parametrization scheme, the large-eddy simulation option in which eddy viscosities are calculated from the prognosed turbulent kinetic energy (Skamarock et al., 2019) is used for turbulent mixing processes. For urban parametrization, the Seoul National University Urban Canopy Model (Ryu et al., 2011) is used, which is coupled with the Noah land surface model in a tile approach. The Seoul National University Urban Canopy Model is a single-layer urban canopy model that considers various physical processes in a street canyon.

Idealized simulations are conducted in a two-dimensional (2-D) domain with a horizontal extent of 500 km and a vertical extent of 6 km. The computational advantage of 2-D settings enables us to conduct a large number of ensemble large-eddy simulations that will be explained later in detail. Meanwhile, it should be noted that the three-dimensional (3-D) aspects of the UBC and convective cells such as cellular convection and convective rolls cannot be represented in two dimensions. The horizontal grid interval is 100 m. A total of 65 vertical layers are used, and 30 of them are in the lowest 2 km of the domain. The vertical grid interval is increased with height from 60 to 169 m. The periodic boundary condition is used at lateral boundaries. To suppress the reflection of gravity waves at the domain top and the growth of poorly resolved features, the Rayleigh damping layer (Klemp et al., 2008) of 2 km and the sixth-order horizontal filter (Knievel

et al., 2007) are applied, respectively. The rotational effect of Earth is ignored. Simulations are performed from 0400 LST June 20 to 0000 LST June 21 (20 hour), with a time step of 0.6 s. The latitude of the domain is set to 30°N at which the sun rises and sets at ~0500 LST and ~1900 LST, respectively, on June 20. Our analyses are mainly focused on the afternoon time (1200–1700 LST), when the UBC and convective cells are well developed.

In the simulation domain, an urban area with a width of 20 km is centered at the domain center and the rest of the domain is rural areas. In the urban area, the fraction of built-up area is 80% and the remaining area is natural area whose land use type is a cropland–grassland mosaic with a vegetation fraction of 0.8 and soil type is loamy sand. The rural area has the land use type of cropland–woodland mosaic with a vegetation fraction of 0.6 and the soil type of loamy sand. The values of the urban parameters and diurnally varying anthropogenic heat flux follow those of Ryu et al. (2013).

To investigate the impacts of background wind on the interactions between the UBC and convective cells, simulations with different initial horizontal wind speeds (from 0 to 5 m·s⁻¹ with the intervals of 0.5 m·s⁻¹) that are homogeneous in the domain are conducted. The initial potential temperature is set to 298 K at $z=0$ m and increases with height at a lapse rate of 5 K·km⁻¹. The initial relative humidity is fixed at 30% in the lowest 4 km and then linearly decreases with height, reaching 10% at the domain top. Note that owing to this low initial humidity, no condensates are formed in any simulation. The locations at which convective cells are generated in the simulations are very sensitive to a small perturbation in the initial condition, which necessitates ensemble simulations to obtain robust results. Fifteen ensemble members are produced by adding random perturbations between -0.1 and +0.1 K to the initial potential temperature at the three lowest levels. Thus, a total of 165 simulations (15 ensemble members for each of the 11 different background wind speeds) are conducted. For comparison, additional 165 ensemble simulations where the urban area is removed are conducted. These additional simulations are named NO-URBAN, and the original simulations are named URBAN.

3 | RESULTS AND DISCUSSION

3.1 | UBC characteristics

In this subsection, how the UBC characteristics change with the background wind speed is examined. Figure 1 shows the ensemble-mean fields of horizontal velocity and potential temperature anomalies along with the ensemble-mean vertical profiles of area-mean horizontal

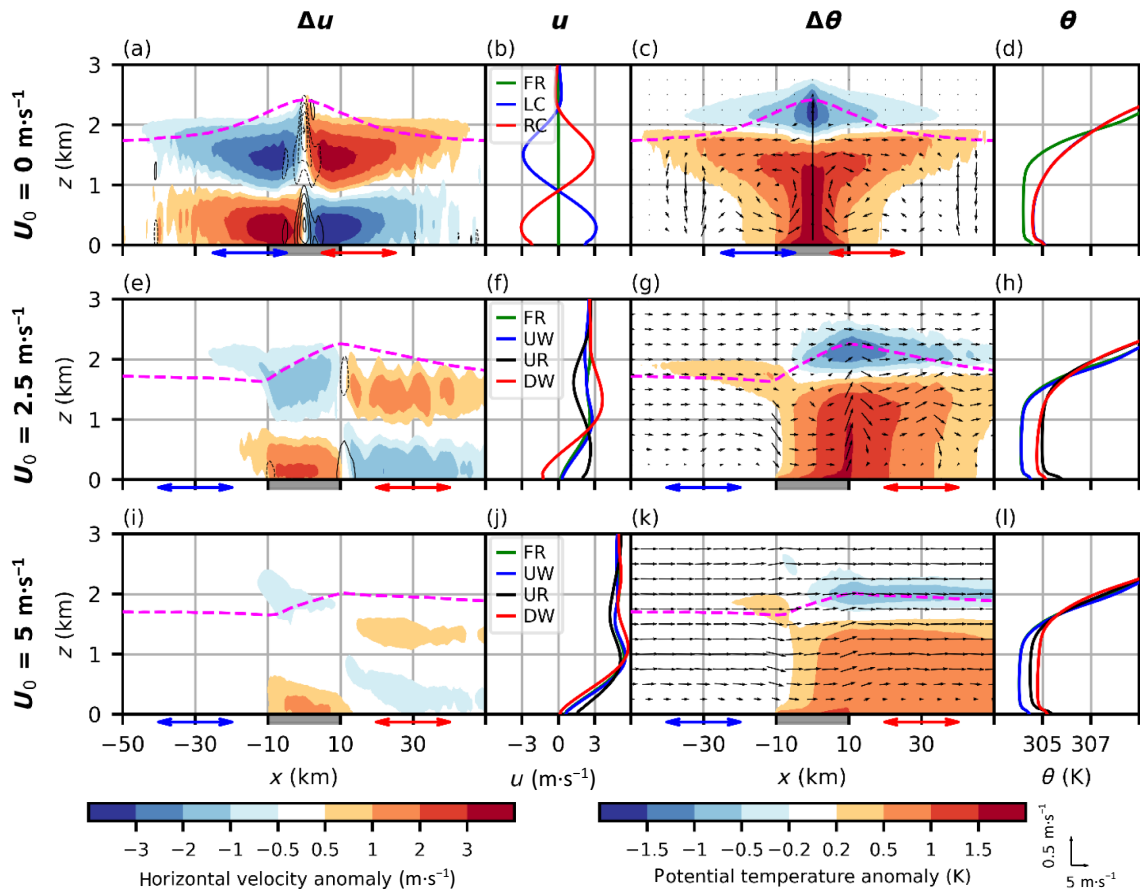


FIGURE 1 Ensemble-mean fields of horizontal velocity anomaly (shades) and 2 km moving-averaged horizontal convergence (black contours) (first column) and those of potential temperature anomaly (shades) and velocity vector (arrows) (third column) with PBL height (pink dashed lines) for $U_0 = 0$ (first row), 2.5 (second row), and $5 \text{ m}\cdot\text{s}^{-1}$ (third row) in the URBAN simulations. The contours for convergence are plotted with $0.4 \times 10^{-3} \text{ s}^{-1}$ intervals except for 0 s^{-1} , and those of negative values are indicated by dashed lines. The UR area is indicated by the gray box on the x axis. Ensemble-mean vertical profiles of area-mean horizontal velocity (second column) and potential temperature (fourth column) for different areas in the same URBAN simulations. The LC and RC areas (first row) and UW and DW areas (second and third rows) are indicated by the two-sided arrows on the x axes of the subfigures in the first and third columns. All variables are averaged over 1200–1700 LST. [Colour figure can be viewed at wileyonlinelibrary.com]

velocity and potential temperature for $U_0 = 0$, 2.5 , and $5 \text{ m}\cdot\text{s}^{-1}$ in the URBAN simulations. Here, the simulation domain is subdivided into the far-upwind (FR, from -250 to -150 km), left UBC (LC, from -25 to -5 km), right UBC (RC, from 5 to 25 km), upwind (UW, from -40 to -20 km), urban (UR, from -10 to 10 km), and downwind (DW, from 20 to 40 km) areas, where the LC and RC areas are only defined when $U_0 = 0 \text{ m}\cdot\text{s}^{-1}$. The anomaly of a variable is calculated by subtracting its horizontal average over the FR area from itself at each height, as the state in the FR area is used as an estimate of the background state. The PBL height is calculated as the height of the maximum vertical gradient of potential temperature. For $U_0 = 0 \text{ m}\cdot\text{s}^{-1}$, circulation and potential temperature anomaly are almost symmetric (Figure 1a,c). The horizontal extent of the UBC is about four times the urban size, which is comparable to those in previous studies summarized in Fan et al. (2017).

The UB converges to the UR area in the lower PBL and diverges from the UR area in the upper PBL (Figure 1a). This reversal of the UB across the PBL produces strong vertical wind shear on both sides of the UBC (Figure 1b). The UBC brings cool air from the rural area in the lower PBL, vertically transports near-surface warm air in the UR area to the upper PBL, and spreads the warm air outward in the upper PBL, resulting in the larger horizontal extent of warm anomaly in the upper PBL than in the lower PBL (Figure 1c). This leads to a larger stability at $z \sim 0.7$ – 1.3 km in the LC and RC areas compared with the background state (Figure 1d).

Figure 2 shows the ensemble-mean UB intensity and UBC center location as a function of U_0 . Here, UB intensity for each ensemble member is defined as the area-mean magnitude of horizontal velocity anomaly averaged over 1200–1700 LST in the lower PBL. The location of the

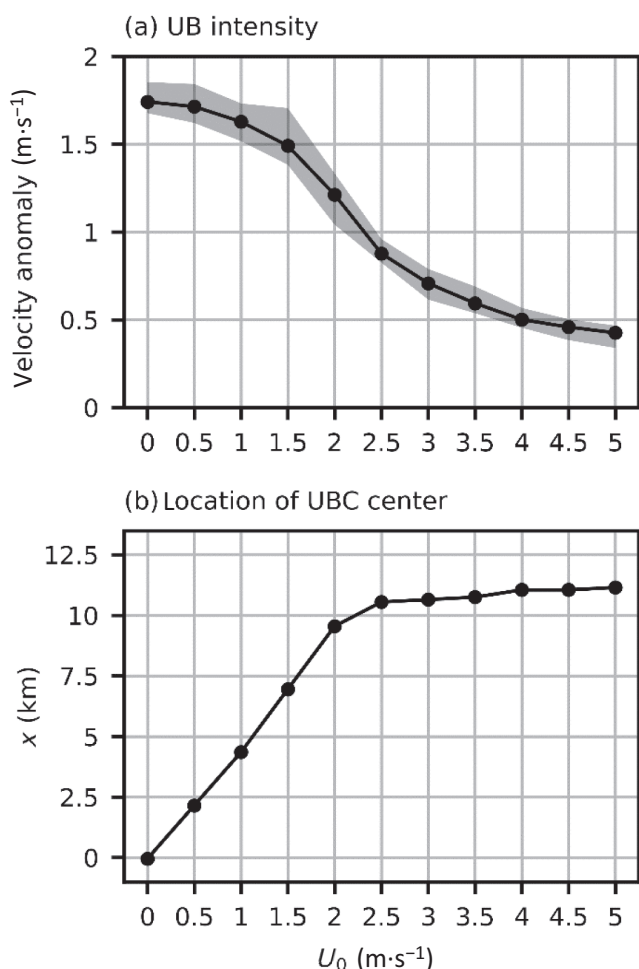


FIGURE 2 (a) Ensemble-mean UB intensity (black line) and (b) location of UBC center as a function of U_0 in the URBAN simulations. The gray shade in (a) indicates the range of UB intensity over all ensemble members.

UBC center is where the direction of lower UB reverses (i.e., where the lower-PBL mean of the horizontal velocity anomaly is closest to zero) in the ensemble-mean fields averaged over 1200–1700 LST. The area for the calculation of the UB intensity for each U_0 is the 40-km area centered at the UBC center. The UB intensity decreases as U_0 increases, and this tendency is consistently found across ensemble members. The location of the UBC center moves downwind as U_0 increases to $2.5 \text{ m}\cdot\text{s}^{-1}$ and almost does not change when U_0 is further increased. These results indicate that the background wind speed greatly influences the UBC characteristics.

For $U_0 = 2.5 \text{ m}\cdot\text{s}^{-1}$, the UB intensity is $0.9 \text{ m}\cdot\text{s}^{-1}$, which is 50% smaller than that for $U_0 = 0 \text{ m}\cdot\text{s}^{-1}$ (Figure 2a), and the UBC center is located near the downwind boundary of the UR area ($x = 10 \text{ km}$) (Figure 2b). Hence, the left part of the UBC is located in the UR area and its right part is located in the DW area (Figure 1e). The lower-PBL convergence is much weaker than that for $U_0 = 0 \text{ m}\cdot\text{s}^{-1}$,

and its maximum is located near the downwind boundary of the UR area. In the DW area, the positive wind shear in the right part of the UBC is superposed on the background wind profile with a positive wind shear (see FR in Figure 1f), resulting in strong shear there. The maximum warm anomaly appears near the downwind boundary of the UR area (Figure 1g). The UW area is not much influenced by the UBC for this U_0 , exhibiting similar vertical profiles of horizontal velocity and potential temperature to those of the background state.

For $U_0 = 5 \text{ m}\cdot\text{s}^{-1}$, the UB intensity is as small as $0.4 \text{ m}\cdot\text{s}^{-1}$, 51% smaller than that for $U_0 = 2.5 \text{ m}\cdot\text{s}^{-1}$ (Figure 2a), and the location of the UBC center is similar to that for $U_0 = 2.5 \text{ m}\cdot\text{s}^{-1}$ (Figure 2b). Owing to the weakened UBC, the convergence in the lower PBL seen in the $U_0 = 0$ and $2.5 \text{ m}\cdot\text{s}^{-1}$ cases is not prominent for this case (Figure 1i). For the same reason, the vertical profiles of horizontal wind in the UW, UR, and DW areas are all similar to that of the background state (Figure 1j), which exhibits a stronger wind shear than the background wind profile for the $U_0 = 2.5 \text{ m}\cdot\text{s}^{-1}$ case. Compared with the $U_0 = 2.5 \text{ m}\cdot\text{s}^{-1}$ case, the warm anomaly has a smaller maximum and is spread further downwind (Figure 1k). For $U_0 = 0$, 2.5 , and $5 \text{ m}\cdot\text{s}^{-1}$, the urban–rural difference in near-surface air temperature is 1.5 , 1.1 , and 0.7°C , respectively, which are in the range of daytime UHI intensity observed in warm seasons (Borbora & Das, 2014; Lee & Baik, 2010; Zhang et al., 2021). The general characteristics of the UBC in the presence and absence of background wind described above are similar to those shown in previous studies (Martilli, 2002; Zhang et al., 2014).

In our simulations, background wind overcomes the lower UB downwind of the UBC center for $U_0 = 2.5 \text{ m}\cdot\text{s}^{-1}$ and substantially inhibits the whole UB for $U_0 = 5 \text{ m}\cdot\text{s}^{-1}$, which is in line with the previous large-eddy simulation studies reporting that background wind of $2\text{--}5 \text{ m}\cdot\text{s}^{-1}$ substantially inhibits surface heterogeneity-induced circulations, including the UBC (Avissar & Schmidt, 1998; Kang & Lenschow, 2014; Lee et al., 2019; Zhang et al., 2014). Note that the lower-PBL background wind speeds in the two cases are 1.3 and $3.1 \text{ m}\cdot\text{s}^{-1}$. These two background wind speeds are respectively about 70% and 180% of the UB intensity for $U_0 = 0 \text{ m}\cdot\text{s}^{-1}$. This suggests that background wind as strong as 70% of the UB under the calm condition is sufficient to overcome the returning lower UB downwind of the UBC center and background wind as strong as 180% of the UB under the calm condition is sufficient to considerably inhibit the whole UB.

Larger surface sensible heat flux in the urban area than in the rural area is responsible for the UBC. How the surface energy fluxes change with different background wind speeds is presented in Figure 3, along with the

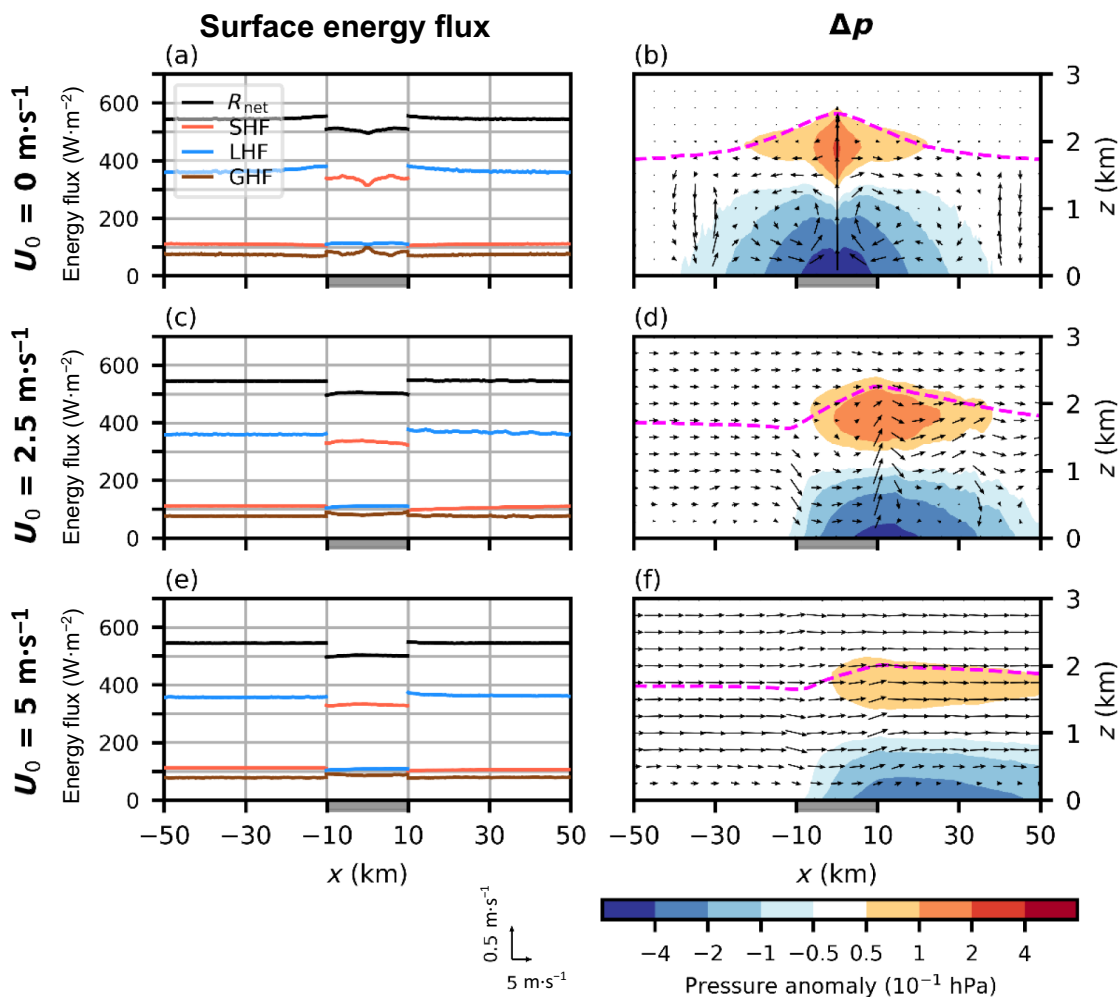


FIGURE 3 (a, c, e) Ensemble-mean horizontal distributions of net radiative flux (R_{net}), sensible heat flux (SHF), latent heat flux (LHF), and ground heat flux (GHF) and (b, d, f) ensemble-mean fields of pressure anomaly (shades) and velocity vector (arrows) with PBL height (pink dashed lines) for U_0 = (a, b) 0, (c, d) 2.5, and (e, f) 5 $\text{m}\cdot\text{s}^{-1}$ in the URBAN simulations. The UR area is indicated by the gray box on the x axis. All variables are averaged over 1200–1700 LST. [Colour figure can be viewed at wileyonlinelibrary.com]

pressure anomaly and wind vector fields. For $U_0 = 0 \text{ m}\cdot\text{s}^{-1}$ (Figure 3a), the net radiative flux is slightly smaller in the UR area than in the rural area due to the larger emission of long-wave radiation from the relatively warm urban surface. In the UR area, this net radiative flux is mainly converted to sensible heat flux, while it is mainly converted to latent heat flux in the rural area. The surface sensible heat flux is $334 \text{ W}\cdot\text{m}^{-2}$ in the UR area and $111 \text{ W}\cdot\text{m}^{-2}$ in the rural area. The surface latent heat flux is $110 \text{ W}\cdot\text{m}^{-2}$ in the UR area and $360 \text{ W}\cdot\text{m}^{-2}$ in the rural area. The calculated Bowen ratio is 3.03 in the UR area and 0.31 in the rural area, which are in the typical ranges of the daytime Bowen ratio for urban areas and croplands, respectively (Oke et al., 2017). The ground heat flux is relatively small in both the UR and rural areas. The overall characteristics of the surface energy balance remain nearly unchanged when U_0 increases (Figure 3a,c,e), which indicates that the surface energy forcing and its urban–rural differences do

not change significantly with the background wind speed in the simulations in this study.

The large sensible heat flux in the urban area heats the overlying air, producing a negative pressure anomaly in the lower PBL and a positive pressure anomaly in the upper PBL. For $U_0 = 0 \text{ m}\cdot\text{s}^{-1}$ (Figure 3b), these pressure anomalies are nearly symmetric, are centered at the urban center, and exhibit relatively stronger maxima. When U_0 increases to $2.5 \text{ m}\cdot\text{s}^{-1}$ (Figure 3d), the pressure anomalies move downwind and their maxima are located near the downwind boundary of the UR area with reduced magnitude, which is consistent with the location of the UBC center (Figure 1e). When U_0 increases from 2.5 to $5 \text{ m}\cdot\text{s}^{-1}$ (Figure 3f), the location of the maximum pressure anomaly in the lower PBL does not change much, like the location of the UBC center (Figure 2b), while the location of the maximum pressure anomaly in the upper PBL moves further downwind by $\sim 6 \text{ km}$. The negative

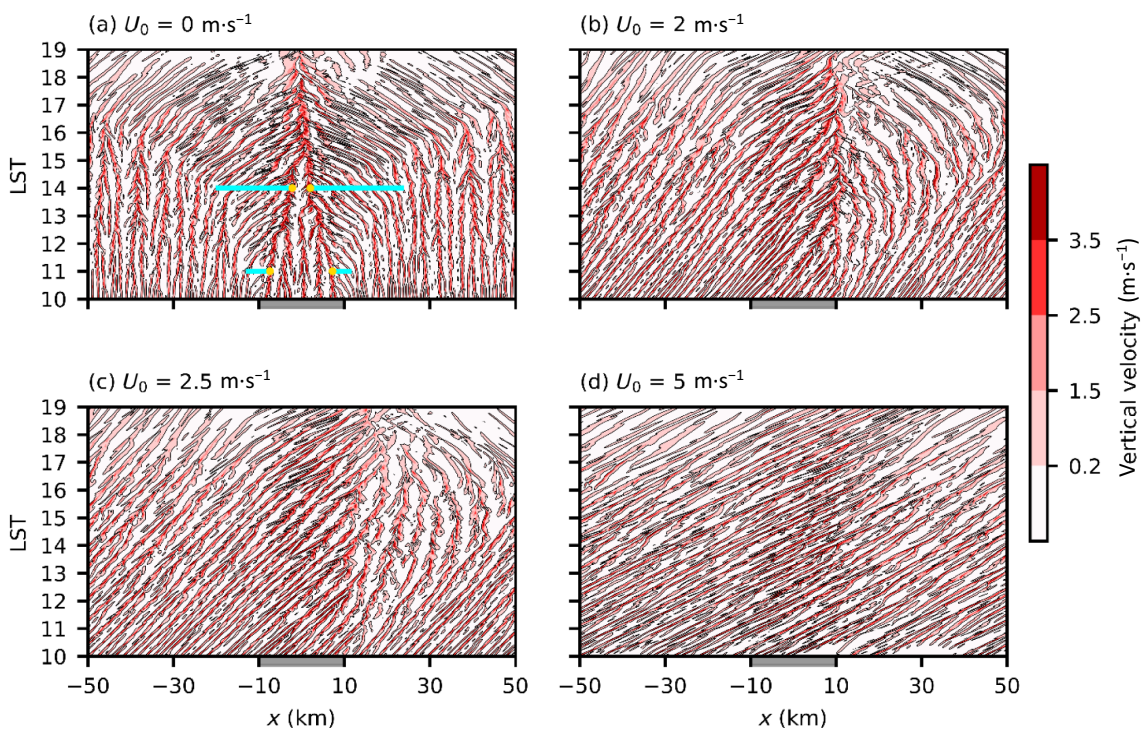


FIGURE 4 Distance–time plots of vertical velocity at $z = 400$ m in a single ensemble member for each of $U_0 =$ (a) 0, (b) 2, (c) 2.5, and (d) $5\text{ m}\cdot\text{s}^{-1}$ in the URBAN simulations. The UR area is indicated by the gray box on the x axis. In (a), the four blue boxes indicate the horizontal extents of the left UB and right UB at 1100 LST and 1400 LST, and the four yellow circles indicate the locations of the UB fronts. [Colour figure can be viewed at wileyonlinelibrary.com]

pressure anomaly in the lower PBL weakens and elongates further downwind, and the magnitude of horizontal pressure gradient decreases. The changes in the pressure anomaly patterns with the background wind speed and the resultant decreases in the magnitude of horizontal pressure gradient lead to the weakening of the UB found in Figures 1 and 2.

3.2 | Convective cells in the UBC

Figure 4 shows the distance–time plots of vertical velocity at $z = 400$ m in a single ensemble member for each of $U_0 = 0, 2, 2.5$, and $5\text{ m}\cdot\text{s}^{-1}$ in the URBAN simulations. In all simulations, convective cells form and compensating downdrafts are present between cell updrafts. The cell wavelengths averaged over 1200–1700 LST are 2.9, 3.0, 3.1, and 4.0 km, respectively, and the aspect ratios averaged over the same period are 1.6, 1.7, 1.8, and 2.3, respectively, for $U_0 = 0, 2, 2.5$, and $5\text{ m}\cdot\text{s}^{-1}$. These values are in the typical ranges reported from the previous overland observations summarized in Banghoff et al. (2020). For $U_0 = 0\text{ m}\cdot\text{s}^{-1}$ (Figure 4a), at 1100 LST, the UB weakly develops near the left and right boundaries of the UR area. The front of the UB near the left (right) boundary of the UR

area is located at the right (left) edge of the UB and is characterized by a relatively strong updraft at that time. As time progresses, the horizontal extent of the UB increases and the left and right UB fronts move toward the urban center. At 1400 LST, the UB covers ~ 41 km and the left and right UB fronts are located at $x = -2.2$ and 2.0 km, respectively. The UB advects convective cells from the rural area toward the urban center. The advected convective cells merge with the UB fronts. Also, as the UB fronts advance toward the urban center, they merge with the convective cells ahead. At 1504 LST, the two UB fronts merge with each other, producing the very strong updraft at the urban center. This updraft continues to merge with the convective cells advected by the UB. The results of the $U_0 = 0\text{ m}\cdot\text{s}^{-1}$ case agree well with those of Ryu et al. (2013).

For $U_0 = 2\text{ m}\cdot\text{s}^{-1}$ (Figure 4b), at 1000 LST, convective cells are advected by the background wind. As time progresses, the UBC develops and a strong updraft forms at its center near the downwind boundary of the UR area. Convective cells advected from the UR area and its upwind repeatedly merge with the strong updraft. Convective cells that originate from the downwind of the UR area move downwind at first but turn toward the UR area as they go under the influence of the UB whose horizontal extent increases with time, and they eventually merge with the

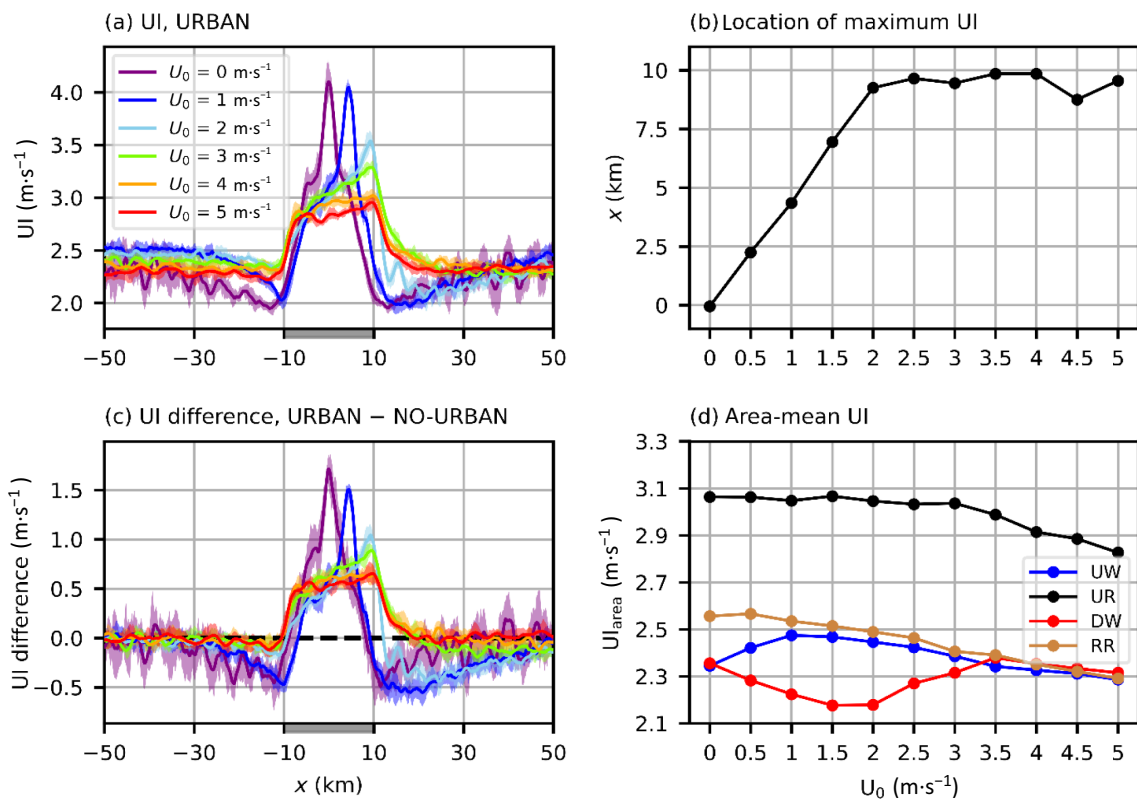


FIGURE 5 (a) Horizontal distributions of ensemble-mean updraft intensity (UI) (lines) for $U_0 = 0, 1, 2, 3, 4$, and $5 \text{ m}\cdot\text{s}^{-1}$ and (b) location of its maximum as a function of U_0 in the URBAN simulations. (c) Differences in ensemble-mean UI between the URBAN and NO-URBAN simulations (lines). (d) Area-mean ensemble-mean UI as a function of U_0 , where “UW”, “UR”, and “DW” indicate the corresponding areas in the URBAN simulations, and the “RR” indicates the 20-km area centered at the domain center in the NO-URBAN simulations. The shades in (a) and (c) indicate the ensemble spreads of UI in the URBAN simulations and UI difference between the URBAN and NO-URBAN simulations, respectively. The UR area is indicated by the gray box on the x axis. All variables are averaged over 1200–1700 LST. [Colour figure can be viewed at wileyonlinelibrary.com]

strong updraft at the UBC center. The $U_0 = 2 \text{ m}\cdot\text{s}^{-1}$ case is similar to the $U_0 = 0 \text{ m}\cdot\text{s}^{-1}$ case in that the strong updraft remains at the UBC center (i.e., near the center of the UR area for $U_0 = 0 \text{ m}\cdot\text{s}^{-1}$ and near the downwind boundary of the UR area for $U_0 = 2 \text{ m}\cdot\text{s}^{-1}$) and convective cells are advected toward the strong updraft and merge with it.

For $U_0 = 2.5 \text{ m}\cdot\text{s}^{-1}$ (Figure 4c), convective cells downwind of the UR area keep moving downwind; even though they are under the influence of the UB, they slowly move downwind until ~ 1600 LST, which is in contrast with the $U_0 = 0$ and $2 \text{ m}\cdot\text{s}^{-1}$ cases. This is because for $U_0 = 2.5 \text{ m}\cdot\text{s}^{-1}$, the background wind overcomes the returning UB downwind of the UBC center that is located near the downwind boundary of the UR area. Convective cells originating from the UR area and the upwind of the UR area move downwind, pass through the UBC center, and decelerate in the downwind of the UR area. Note that while the strong updraft at the UBC center for $U_0 = 0$ and $2 \text{ m}\cdot\text{s}^{-1}$ remains there, the strong updraft at the UBC center for $U_0 = 2.5 \text{ m}\cdot\text{s}^{-1}$ moves downwind and is replaced by another strong updraft approaching from its

upwind. For $U_0 = 5 \text{ m}\cdot\text{s}^{-1}$ (Figure 4d), the movements of convective cells are hardly affected by the UB, as the UB is substantially weak in the $U_0 = 5 \text{ m}\cdot\text{s}^{-1}$ case compared with the $U_0 = 2.5 \text{ m}\cdot\text{s}^{-1}$ case. All cells are advected downwind mainly by the background wind.

Figure 5 shows the horizontal distributions of ensemble-mean updraft intensity and the location of its maximum in the URBAN simulations, its difference between the URBAN and NO-URBAN simulations, and the area-mean ensemble-mean updraft intensity of different areas in the URBAN and NO-URBAN simulations. To obtain the horizontal distributions in Figure 5a, the maximum vertical velocity in the PBL that is larger than $1 \text{ m}\cdot\text{s}^{-1}$ at each horizontal grid point is time-averaged and then ensemble-averaged. Then, a 2-km moving average is taken. The ensemble spread is represented by the 25–75th percentile range of ensemble members in Figure 5a,c. As U_0 increases from 0 to $2 \text{ m}\cdot\text{s}^{-1}$, the peak in the horizontal distribution of updraft intensity is lowered and its location moves from the urban center to the downwind boundary of the UR area (Figure 5a,b). As U_0 further increases to

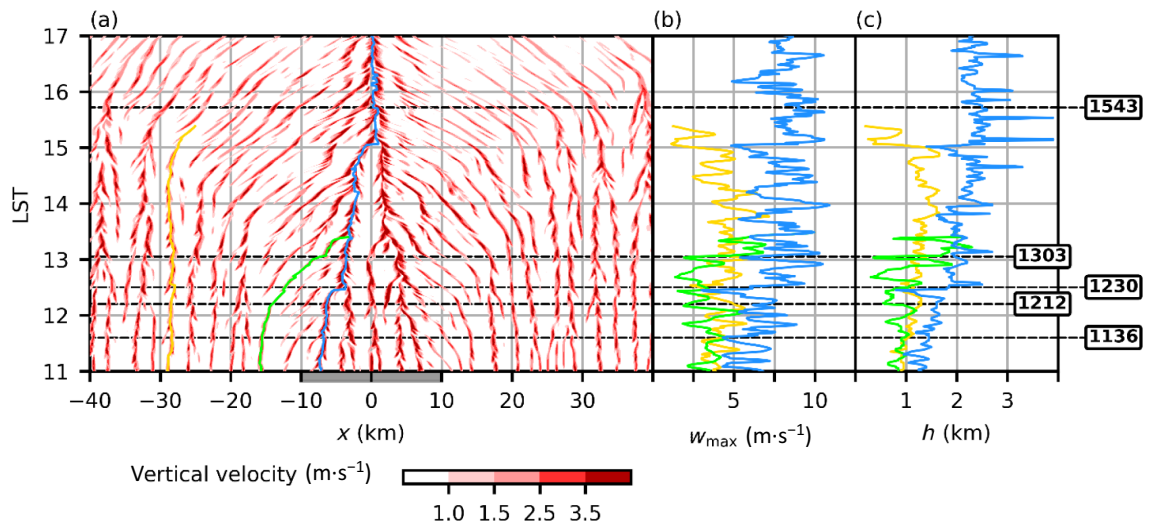


FIGURE 6 Temporal changes of the (a) locations, (b) maximum vertical velocities, and (c) vertical extents of the left UB front updraft (C1, blue line) and two cell updrafts (C2, green line; C3, yellow line) in a single ensemble member for $U_0 = 0 \text{ m}\cdot\text{s}^{-1}$ in the URBAN simulations. The updraft locations are overlaid on the distance–time plot of vertical velocity at $z = 400$ m. The UR area is indicated by the gray box on the x axis. The dashed lines indicate specific times (LST) given in the black boxes. [Colour figure can be viewed at wileyonlinelibrary.com]

5 $\text{m}\cdot\text{s}^{-1}$, the horizontal distribution changes from a distribution with a prominent peak to a hat-like distribution and the maximum updraft intensity remains near the downwind boundary of the UR area. The relatively narrow ensemble spread compared with the gap between the horizontal distributions in the UR area and nearby rural areas indicates that the characteristic change in horizontal distribution appears in overall ensemble members.

Baik et al. (2001) and Han and Baik (2008) conducted numerical simulations of UHI-induced flows where the surface process is turned off and the UHI is prescribed to have a structure that is bell-shaped in the horizontal and exponentially decays in the vertical. The two studies show that a strong updraft induced by a UHI appears downwind of the urban center, which is consistent with the result of this study. The studies also show that the strong updraft is located further downwind with increasing background wind speed. This is different from the result of this study (Figure 5b). It should be noted that in Baik et al. (2001) and Han and Baik (2008), the prescribed horizontal heating structure is continuous (there is no clear boundary between the urban and surrounding rural areas) and convective cells are not produced because of the experimental set-up.

The comparison between the URBAN and NO-URBAN simulations in Figure 5c,d shows the urban effects on convective cell updrafts in different areas. For $U_0 = 0 \text{ m}\cdot\text{s}^{-1}$, the updraft intensity in the URBAN simulations is substantially larger at the urban center but smaller in the nearby rural areas than that in the NO-URBAN simulations, which indicates that the convective updrafts in the nearby

rural areas are suppressed by the urban effect (Figure 5c). Because the urban-induced suppression effect takes place further downwind as U_0 increases, the suppression of updrafts in the upwind of the UR area is substantially reduced while that in the downwind of the UR area remains. The suppression effect is apparent in the majority of ensemble members for $U_0 \leq 2 \text{ m}\cdot\text{s}^{-1}$, as shown by the interquartile range of difference between the URBAN and NO-URBAN simulations being below zero in those areas. When U_0 increases further, the suppression effect almost disappears in both the upwind and downwind of the UR area. This urban-induced suppression effect can also be seen from Figure 5d. It is prominent in the UW area for $U_0 \leq 0.5 \text{ m}\cdot\text{s}^{-1}$ and in the DW area for $U_0 \leq 3 \text{ m}\cdot\text{s}^{-1}$. This leads to a weaker updraft intensity in the DW area than in the UW area for $U_0 = 0.5\text{--}3.0 \text{ m}\cdot\text{s}^{-1}$.

3.3 | Interactions between the UBC and convective cells

In this subsection, we trace individual convective cells that are merging or tilting under the influence of the UBC to further understand the UBC–convective cell interactions under different background wind speeds. In a single ensemble member for each of $U_0 = 0, 2.5$, and $5 \text{ m}\cdot\text{s}^{-1}$ in the URBAN simulations, the temporal evolutions of individual cells or the UB front are examined. Figure 6 shows the temporal changes of the locations, maximum vertical velocities, and vertical extents of the updraft of the left UB front (C1) and two cell updrafts (C2 and C3) for

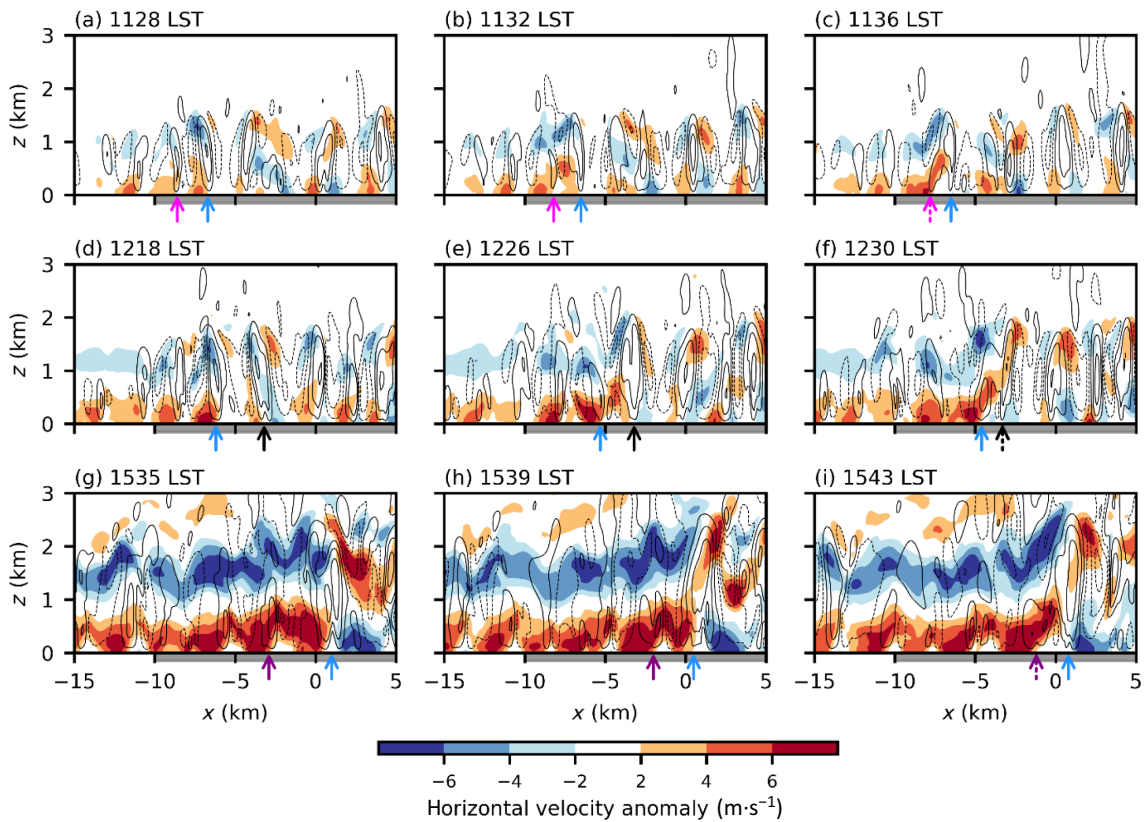


FIGURE 7 Fields of horizontal velocity anomaly (shades) and vertical velocity (contours) at different times between 1128 LST and 1543 LST in a single ensemble member for $U_0 = 0 \text{ m}\cdot\text{s}^{-1}$ in the URBAN simulations, where the location of C1 is indicated by the blue arrow. The arrows of other colors indicate examples of other cell updrafts that interact with C1 (see the text). The dashed arrows indicate the cell updrafts that have merged with C1. The contours for vertical velocity are plotted at $-6, -3, -1, +1, +3$, and $+6 \text{ m}\cdot\text{s}^{-1}$, and those of negative values are indicated by dashed lines. The UR area is indicated by the gray box on the x axis. [Colour figure can be viewed at wileyonlinelibrary.com]

$U_0 = 0 \text{ m}\cdot\text{s}^{-1}$. Here, the updrafts are identified by the areas on the x - z plane where the vertical velocity is larger than $1 \text{ m}\cdot\text{s}^{-1}$. C2 is the updraft of a convective cell that originates from the rural area, which is advected toward the UR area and merges with the updraft of the left UB front (C1). C3 is the updraft of a convective cell that remains in the rural area until it dissipates. Overall, the maximum vertical velocity and vertical extent of C1 are much larger than those of C2 and C3 (Figure 6b,c).

Figure 7 shows the temporal evolution of C1 during 1128–1543 LST in terms of horizontal velocity anomaly and vertical velocity in the $U_0 = 0 \text{ m}\cdot\text{s}^{-1}$ case. At 1128 LST (Figure 7a), the left UB front (C1, blue arrow) is located at $x = -6.7 \text{ km}$ and weak UB is present on the left of the front. A cell located on the left of C1 (pink arrow) is advected toward C1 by the UB (Figure 7a,b) and its updraft merges with C1 at 1136 LST (Figure 7c). This merger intensifies C1, which is represented in Figure 6b as the abrupt increase in maximum vertical velocity of C1 (by $3.2 \text{ m}\cdot\text{s}^{-1}$) right after the merger. As time progresses, C1 advances toward the urban center (Figure 7d,e) and merges with a cell updraft in the UR area at 1230 LST (black arrow)

(Figure 7f). Right after this merger, the maximum vertical velocity and vertical extent of C1 increase by $3.2 \text{ m}\cdot\text{s}^{-1}$ and 0.6 km , respectively (Figure 6b,c). The left UB front (C1) merges with the right UB front, producing the very strong updraft at the UBC center at 1504 LST (Figure 6a). This strong updraft keeps merging with the updrafts of the cells advected by the UB, as exemplified by the merger at 1543 LST (Figure 7i). Right after this merger, the maximum vertical velocity of C1 increases by $1.1 \text{ m}\cdot\text{s}^{-1}$ (Figure 6b). The strong updraft at the UBC center accounts for the peak of updraft intensity at the urban center for $U_0 = 0 \text{ m}\cdot\text{s}^{-1}$ (Figure 5a). The enhancement of the UBC updraft due to the mergers with cell updrafts resembles frontal updraft enhancements that are found in sea breeze simulations when the frontal updraft merges with cell updrafts (Jiang et al., 2017; Ogawa et al., 2003).

The temporal evolution of C2 during 1204–1324 LST is presented in Figure 8. C2 (green arrow) is originally located in the rural area. As the horizontal extent of the UB increases and the UB begins to influence C2, C2 tilts downshear (Figure 8a,b) and weakens (Figure 8c). The UB-induced weakening makes C2 weaker than C3

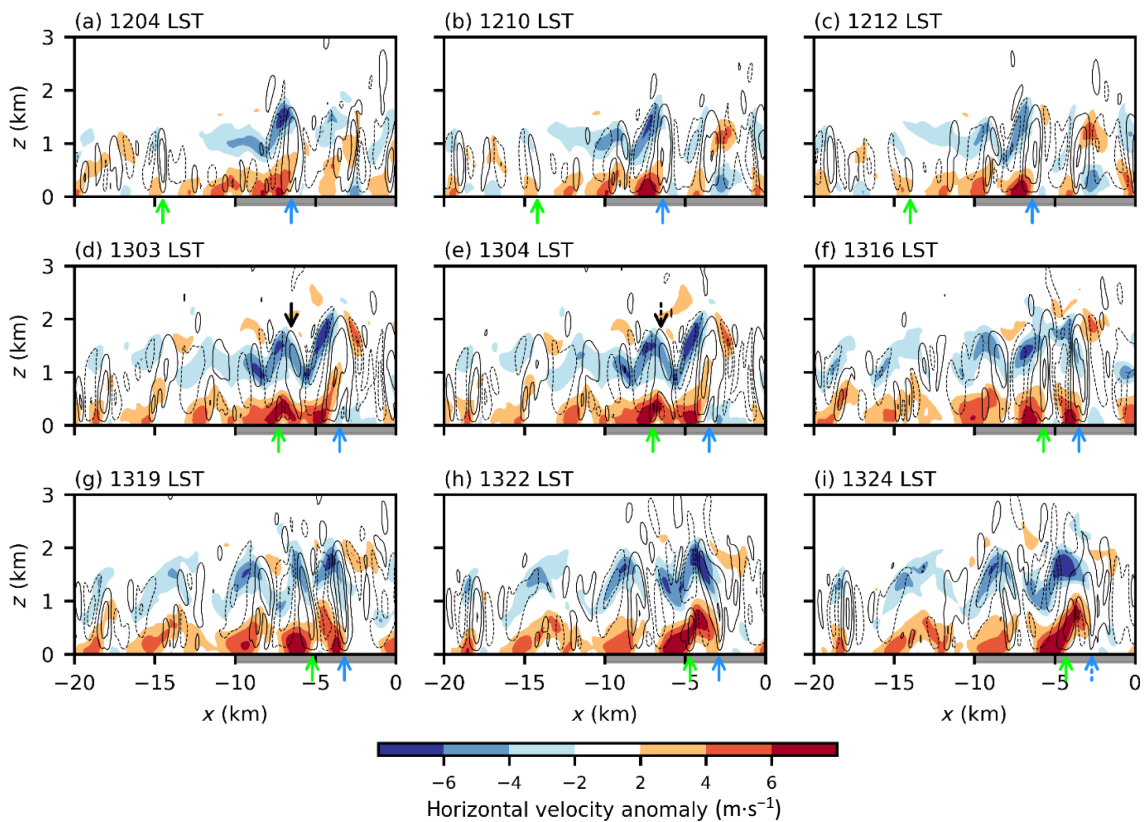


FIGURE 8 As in Figure 7, but for times between 1204 LST and 1324 LST. The location of C2 is additionally indicated by the green arrow. The black arrow indicates an example of a cell updraft that interacts with C2 (see the text). The dashed arrows indicate the cell updrafts that have merged with C2. [Colour figure can be viewed at wileyonlinelibrary.com]

while C2 travels in the areas near the urban boundary (Figure 6b), consistent with the urban-induced suppression of updrafts there shown in Figure 5c. C2 is advected toward the urban center by the UB and merges with a cell updraft in the UR area (black arrow) at 1304 LST (Figure 8e). The merged cell updraft (C2) intensifies and grows (Figure 8f). C2 then tilts downshear (Figure 8g), weakens (Figure 8h), and merges with the updraft of the left UB front (C1, blue arrow) (Figure 8i), enhancing it. Other convective cells advected from the rural area also experience similar processes as C2 and contribute to intensifying the updraft of the UB front or the strong updraft at the UBC center. Note that the interactions between the UBC and convective cells in the cases with U_0 up to $2\text{ m}\cdot\text{s}^{-1}$ are similar to those found in the $U_0=0\text{ m}\cdot\text{s}^{-1}$ case (not shown), although the location of the UBC center moves downwind as U_0 increases.

Figure 9 shows the temporal changes of the locations, maximum vertical velocities, and vertical extents of three cell updrafts (C4, C5, and C6) for $U_0=2.5\text{ m}\cdot\text{s}^{-1}$. C4 is the updraft of a cell that originates from the upwind of the UR area, which passes the UR area and dissipates in the downwind of the UR area. C5 and C6 are the updrafts of cells that originate from the downwind and far upwind of

the UR area, respectively. The maximum vertical velocity and vertical extent of C4 become significantly larger than those of C5 and C6 after 1411 LST, when C4 travels in the downwind part of the UR area.

The temporal evolution of C4 during 1300–1534 LST is presented in Figure 10. At 1300 LST, C4 (blue arrow) is located in the upwind part of the UR area (Figure 10a). It merges with a cell updraft (black arrow) approaching from its upwind at 1303 LST (Figure 10b), and it intensifies and grows after the merger (Figures 9b,c and 10c). As C4 moves downwind, it merges with cell updrafts located at its downwind, as exemplified by the merger at 1411 LST (Figure 10e). Right after this merger, the maximum vertical velocity and vertical extent of C4 increase by $3.2\text{ m}\cdot\text{s}^{-1}$ and 0.4 km , respectively (Figure 9b,c), becoming the strongest cell updraft in the whole simulation domain (Figure 10f). While C4 travels in the downwind part of the UR area, C4 maintains its intensity and repeatedly merges with other cell updrafts (not shown). C4 weakens after it passes the downwind boundary of the UR area (1506 LST). The downshear tilting and substantial weakening of C4 that occur during 1525–1534 LST (Figure 10g–i) make it no longer the strongest cell updraft in the domain (Figure 9a). During this period, the maximum vertical velocity and vertical extent of C4 decrease by $1.8\text{ m}\cdot\text{s}^{-1}$ and 0.5 km , respectively

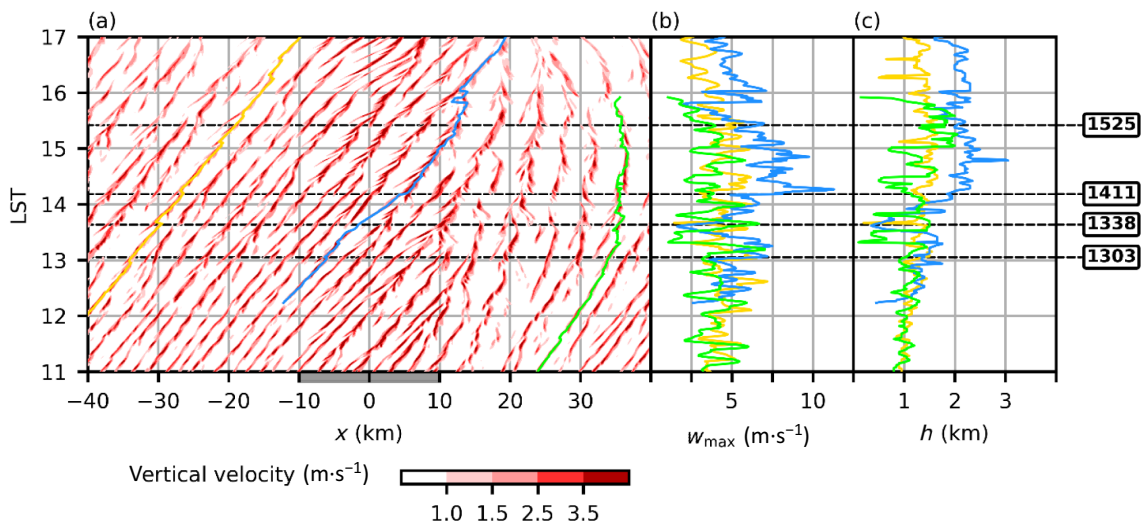


FIGURE 9 As in Figure 6, but for three cell updrafts (C4, blue line; C5, green line; C6, yellow line) in a single ensemble member for $U_0 = 2.5 \text{ m}\cdot\text{s}^{-1}$ in the URBAN simulations. [Colour figure can be viewed at wileyonlinelibrary.com]

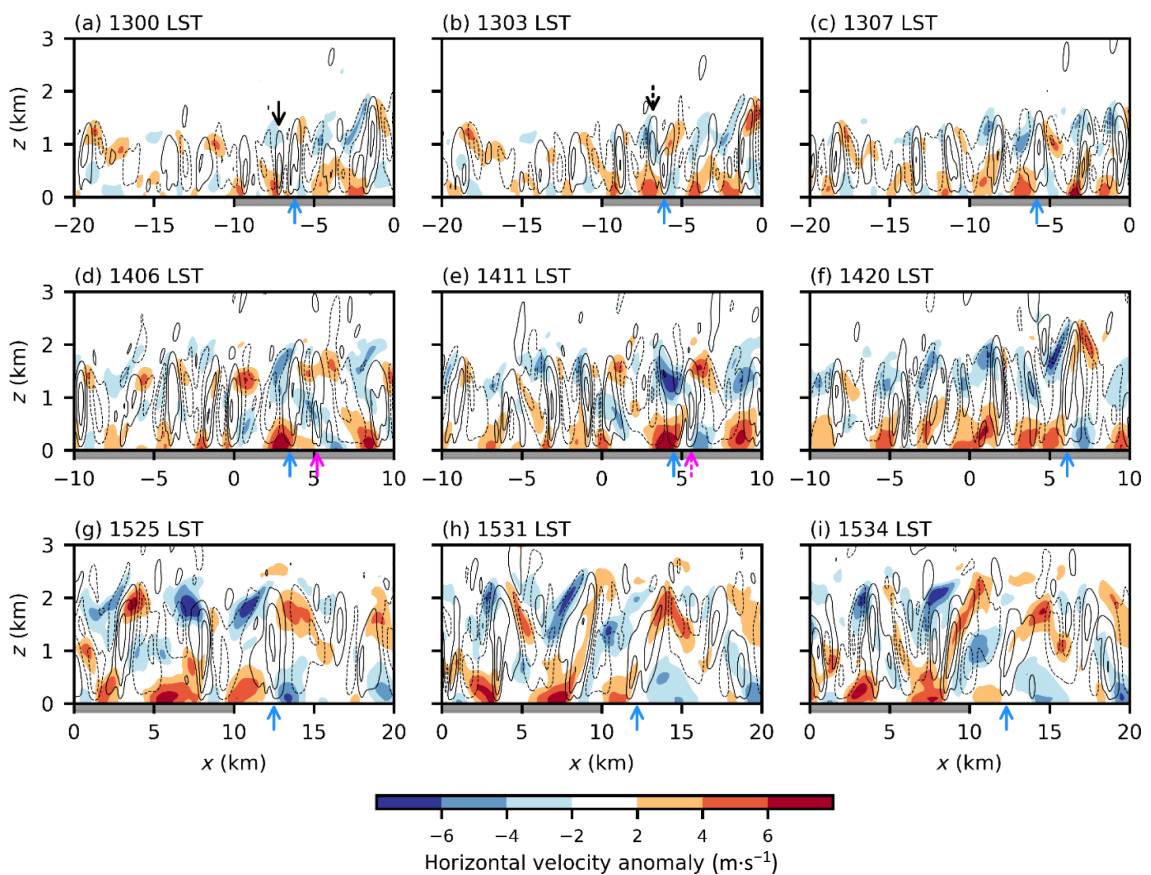


FIGURE 10 As in Figure 7, but for times between 1300 LST and 1534 LST in a single ensemble member for $U_0 = 2.5 \text{ m}\cdot\text{s}^{-1}$ in the URBAN simulations. The location of C4 is indicated by the blue arrow. The arrows of other colors indicate examples of a cell updraft that interacts with C4 (see the text). The dashed arrows indicate the cell updrafts that have merged with C4. [Colour figure can be viewed at wileyonlinelibrary.com]

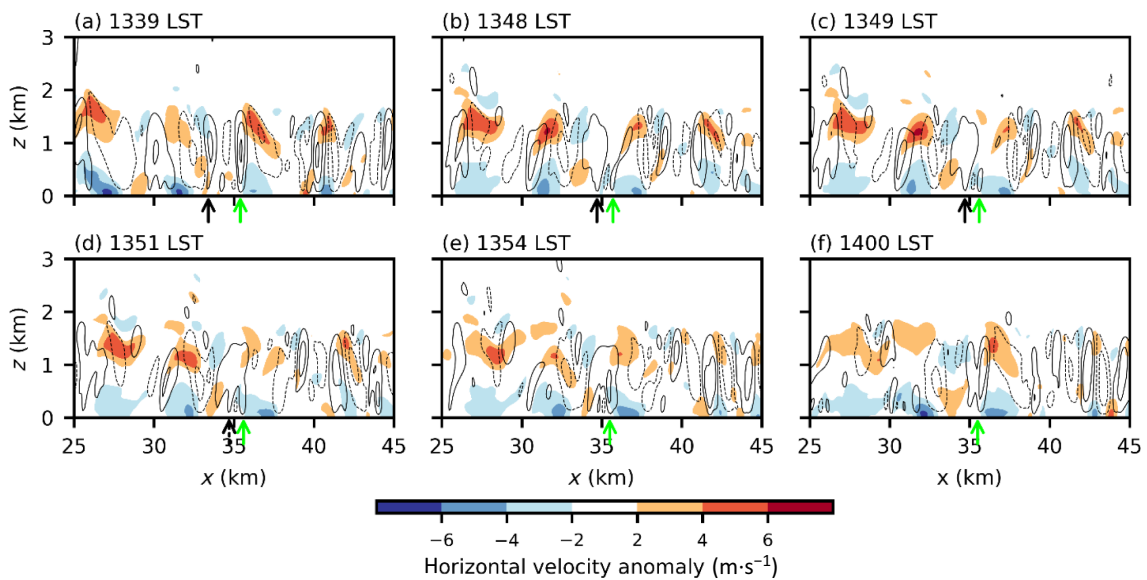


FIGURE 11 As in Figure 7, but for times between 1339 LST and 1400 LST in a single ensemble member for $U_0 = 2.5 \text{ m}\cdot\text{s}^{-1}$ in the URBAN simulations. The location of C5 is indicated by the green arrow. The black arrow indicates an example of other cell updrafts that interact with C5 (see the text). The dashed arrow indicates the cell updraft that has merged with C5. [Colour figure can be viewed at wileyonlinelibrary.com]

(Figure 9b,c). After experiencing similar tilting and weakening several times in the downwind area, C4 eventually dissipates at 1711 LST (not shown). The strong updrafts of the convective cells passing the downwind part of the UR area account for the strong updraft intensity near the downwind boundary of the UR area for $U_0 = 2.5 \text{ m}\cdot\text{s}^{-1}$ (Figure 5a).

Figure 11 shows the temporal evolution of C5 during 1339–1400 LST. During this period, C5 is under the influence of the UB and almost maintains its location at $x \sim 35.5 \text{ km}$. Note that the DW area that includes this location exhibits a strong positive wind shear in the PBL resulting from the superposition of the positive wind shear in the right part of the UBC over the positive wind shear of the background wind profile (Figure 1f). In the DW area, C5 that is upright at 1339 LST (Figure 11a) tilts and weakens at 1348–1349 LST (Figure 11b,c). Then, the weakened C5 merges with a cell updraft approaching from the upwind direction (black arrow) (Figure 11d) and intensifies again (Figure 11e,f). C5 repeatedly experiences similar tilting, weakening, and re-intensifying (not shown) until it dissipates at 1555 LST (Figure 9a). The maximum vertical velocity of C5 during 1330–1530 LST is smaller than that of C6 (Figure 9b), which is consistent with relatively strong urban-induced suppression of updrafts in the DW area compared with that in the UW area for $U_0 = 2.5 \text{ m}\cdot\text{s}^{-1}$ (Figure 5d).

Figure 12 shows the temporal changes of the locations, maximum vertical velocities, and vertical extents of two cell updrafts (C7 and C8) for $U_0 = 5 \text{ m}\cdot\text{s}^{-1}$. C7 is the updraft

of a cell that originates from the upwind of the UR area, which passes the UR area and dissipates in its downwind. C8 is the updraft of a cell that originates from further upwind than C7 and dissipates in the downwind part of the UR area. During 1345–1430 LST, when C7 travels in the downwind part of the UR area and the downwind of the UR area and C8 travels in the upwind of the UR area, the maximum vertical velocity and vertical extent of C7 are considerably larger than those of C8. During 1445–1545 LST, when C7 travels in the DW area and C8 travels in the UR area, the vertical extent of C7 is similar to that of C8 while the maximum vertical velocity of C7 is smaller than that of C8. The overall difference in maximum vertical velocity between C7 and C8 is relatively small compared with that between the traced cell updrafts for $U_0 = 0$ and $2.5 \text{ m}\cdot\text{s}^{-1}$.

Figure 13 shows the temporal evolution of C7 during 1123–1323 LST. Note that for $U_0 = 5 \text{ m}\cdot\text{s}^{-1}$, the whole domain exhibits a strong positive wind shear in the PBL due to the strong background wind (Figure 1j). When C7 travels in the upwind of the UR area, it repeatedly experiences tilting, weakening (Figure 13a–c), and re-intensifying. This is represented as the prominent oscillations of its maximum vertical velocity and vertical extent during 1100–1230 LST in Figure 12b,c. After C7 enters the UR area, it tilts (Figure 13d,e), weakens (Figure 13f), and merges with another cell updraft (black arrow) (Figure 13g–i), which makes the fluctuations of its maximum vertical velocity stronger than before it enters the UR area (Figure 12b). When C7 travels

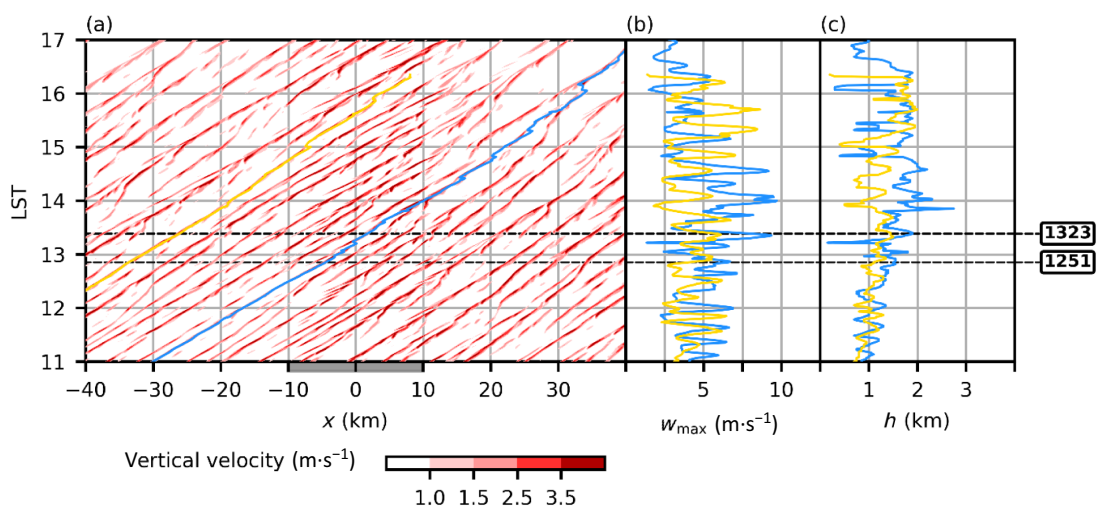


FIGURE 12 As in Figure 6, but for two cell updrafts (C7, blue line; C8, yellow line) in a single ensemble member for $U_0 = 5 m \cdot s^{-1}$ in the URBAN simulations. [Colour figure can be viewed at wileyonlinelibrary.com]

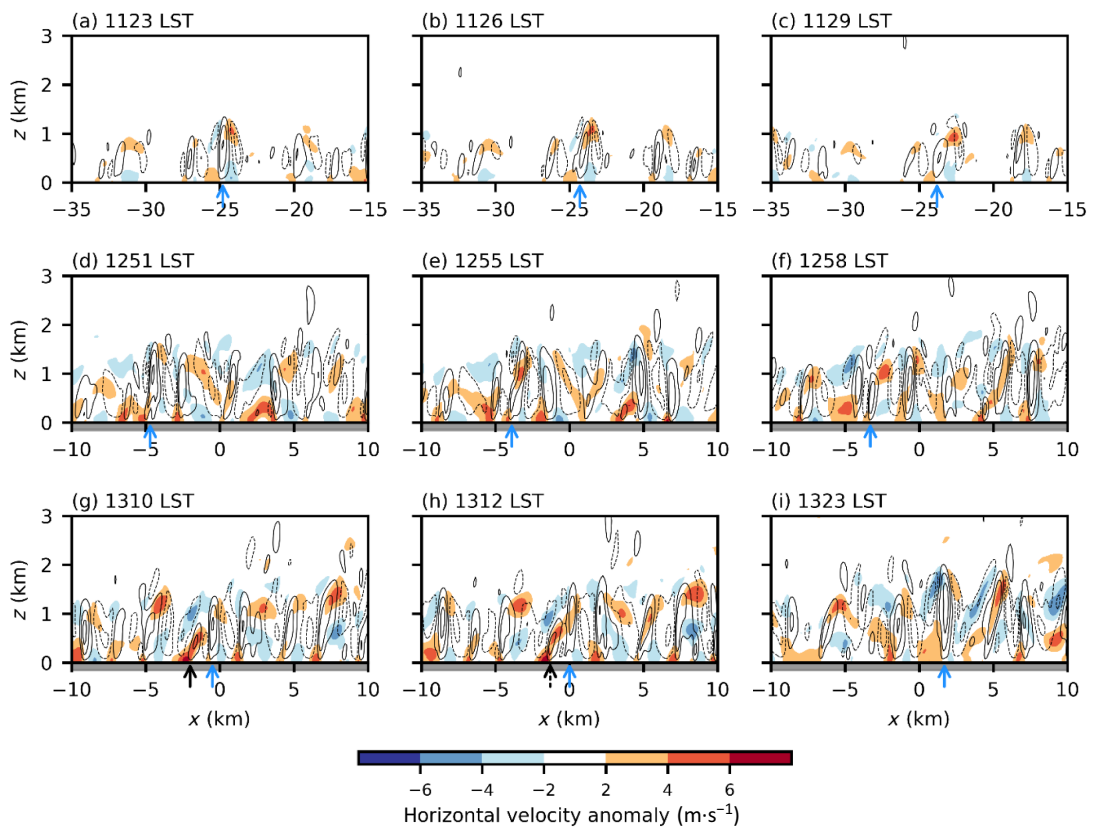


FIGURE 13 As in Figure 7, but for times between 1123 LST and 1323 LST in a single ensemble member for $U_0 = 5 m \cdot s^{-1}$ in the URBAN simulations. The location of C7 is indicated by the blue arrow. The black arrow indicates an example of other cell updrafts that interact with C7 (see the text). The dashed arrow indicates the cell updraft that has merged with C7. [Colour figure can be viewed at wileyonlinelibrary.com]

in the UR area, its maximum vertical velocity is larger than that of C8 which is located in the upwind of the UR area. This is consistent with the stronger updraft intensity in the UR area than in the upwind of the UR area for $U_0 = 5 m \cdot s^{-1}$ (Figure 5a). After C7 leaves the UR

area, it continues to experience tilting, weakening, and re-intensifying until it dissipates in the far downwind of the UR area.

The intensification and weakening of individual convective cells associated with their merging and tilting

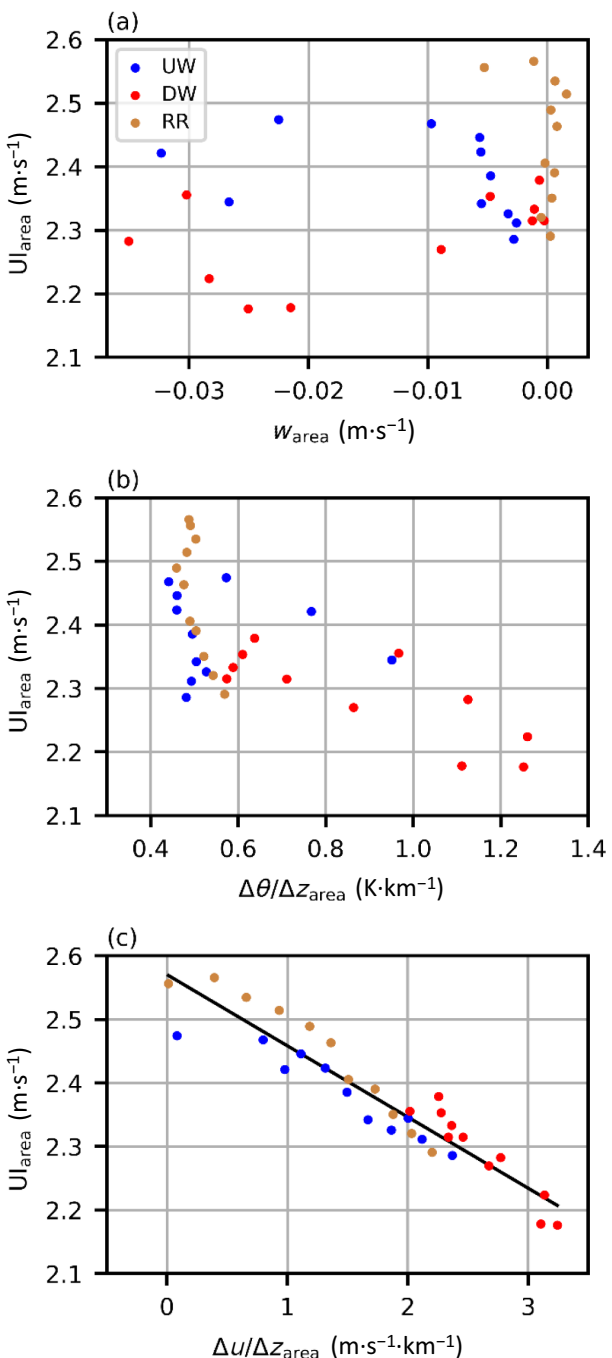


FIGURE 14 Scatter plots of the area-mean ensemble-mean updraft intensities against the area-mean ensemble-mean (a) vertical velocity, (b) vertical gradient of potential temperature, and (c) vertical wind shear for the UW, DW, and RR areas. [Colour figure can be viewed at wileyonlinelibrary.com]

examined earlier herein contribute to constructing the characteristic horizontal distribution of updraft intensity for each background wind speed shown in Figure 5. The differences in these cell behaviors under different background wind speeds induce the changes in the updraft intensity distribution with the background wind speed.

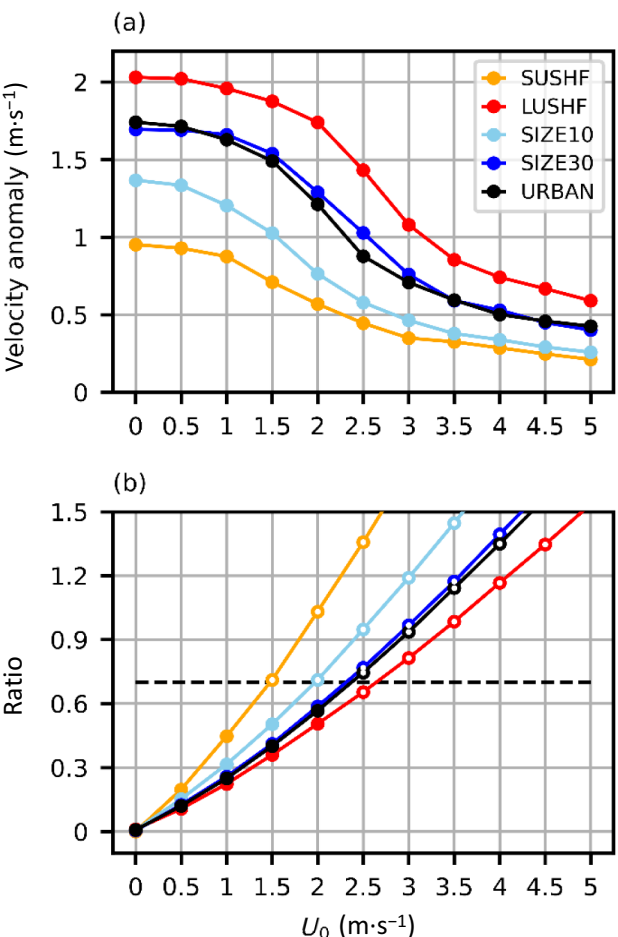


FIGURE 15 (a) Ensemble-mean UB intensity and (b) ratio of ensemble-mean lower-PBL background wind speed to the ensemble-mean UB intensity for $U_0 = 0 \text{ m}\cdot\text{s}^{-1}$ as a function of U_0 in the SUSHF, LUSHF, SIZE10, SIZE30, and URBAN simulations. The opened circles in (b) indicate the cases in which lower-PBL wind averaged over 5–25 km downwind of the UBC center is directed downwind. The dashed line in (b) indicates the ratio of 0.7. [Colour figure can be viewed at wileyonlinelibrary.com]

The downshear tilting and subsequent weakening of cells are mainly found in the areas near the urban boundary for $U_0 = 0 \text{ m}\cdot\text{s}^{-1}$ and in the DW area for $U_0 = 2.5 \text{ m}\cdot\text{s}^{-1}$. For $U_0 = 0$ and $2.5 \text{ m}\cdot\text{s}^{-1}$, these areas are where the urban-induced suppression of updrafts occurs and where relatively strong wind shear appears. This suggests that the strong wind shear can be responsible for the downshear tilting of convective cells and their subsequent weakening composes the urban-induced suppression of updrafts. Meanwhile, Ryu et al. (2013), who also reported the weakening of cell updrafts under the influence of the UBC, suggested two other possible factors contributing to the weakening. One is the downward motion associated with the UBC, and the other is the large static stability due to the transport of warm air to the upper

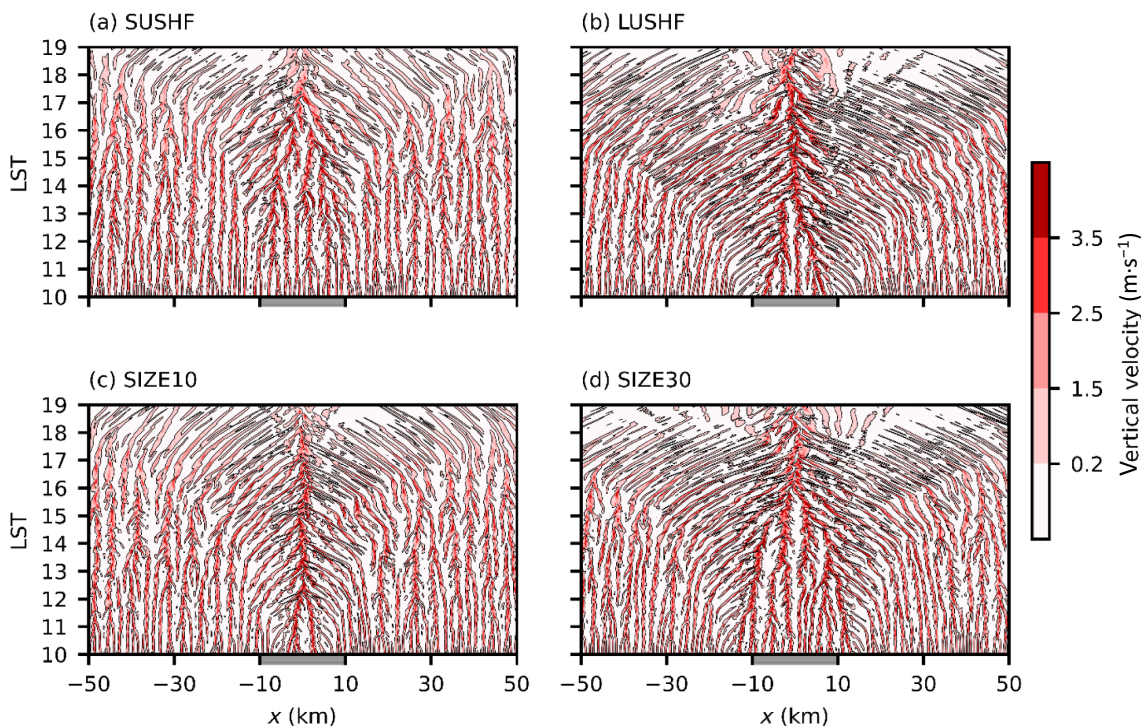


FIGURE 16 Distance–time plots of vertical velocity at $z = 400$ m in a single ensemble member for $U_0 = 0$ $\text{m} \cdot \text{s}^{-1}$ in the (a) SUSHF, (b) LUSHF, (c) SIZE10, and (d) SIZE30 simulations. [Colour figure can be viewed at wileyonlinelibrary.com]

PBL by the UBC. To examine which factor is more closely tied to the urban-induced suppression effect, how the updraft intensity is related to the three factors needs to be investigated.

The scatter plots of area-mean updraft intensities against area-mean vertical velocity, vertical gradient of potential temperature, and vertical wind shear are shown in Figure 14. The vertical gradient of potential temperature is used as a measure of static stability, and it is calculated as the difference in potential temperature between its upper-PBL and lower-PBL means divided by the half of the PBL height. The vertical wind shear is calculated as the absolute difference in horizontal velocity between its upper-PBL and lower-PBL means divided by the half of the PBL height. The vertical velocities in the UW and DW areas in the URBAN simulations are all negative, reflecting the downward motion associated with the UBC (Figure 14a). However, no systematic relationship is found between the vertical velocity and the updraft intensity. For the static stability, its relationship with the updraft intensity in the DW area is close to linear, but no such relationship is found in the UW and RR areas (Figure 14b). The vertical wind shear shows a clear linear relationship with the updraft intensity (Figure 14c), with the coefficient of determination R^2 and the slope being 0.89 and $-0.11 \text{ m} \cdot \text{s}^{-1} \cdot (\text{m} \cdot \text{s}^{-1} \cdot \text{km}^{-1})^{-1}$, respectively. This value of R^2 is much larger than those for the vertical

velocity (0.13) and the static stability (0.45). The fact that the updraft intensity is strongly correlated with the vertical wind shear indicates that the urban-induced suppression of updrafts can be mainly associated with the strong vertical wind shear due to the UB, rather than with other factors.

3.4 | Sensitivities to urban sensible heat flux and urban size

In the previous subsections, we examined how the UBC characteristics, convective cells in the UBC, and their interactions change with background wind speed. In this subsection, we examine the sensitivity of those results to urban characteristics such as the surface sensible heat flux and urban size. To represent different magnitudes of urban surface sensible heat flux, the albedo of the surfaces in the built-up area and the built-up area fraction are changed from (0.2, 0.8) to (0.3, 0.6) and (0.1, 1.0). Two additional sets of ensemble simulations are conducted with a smaller urban surface sensible heat flux and a larger urban surface sensible heat flux and are named SUSHF and LUSHF, respectively. The urban surface sensible heat flux averaged over the urban area (UR area) during 1200–1700 LST in the SUSHF and LUSHF simulations are 220 and 471 $\text{W} \cdot \text{m}^{-2}$, respectively, which are the values decreased by

34% and increased by 41% from that in the URBAN simulations ($334 \text{ W}\cdot\text{m}^{-2}$), respectively. In addition, two sets of ensemble simulations with the urban area's widths of 10 and 30 km are also conducted and are named SIZE10 and SIZE30, respectively.

The ensemble-mean UB intensity in the sensitivity and URBAN simulations as a function of U_0 is plotted in Figure 15a. As U_0 increases, the UB weakens in all simulations. The SUSHF simulations exhibit weaker UB than the URBAN simulations, while the LUSHF simulations exhibit stronger UB. The SIZE10 simulations have smaller UB intensity than the URBAN simulations, while the SIZE30 simulations have UB intensity similar to that in the URBAN simulations. Similarity in the weakening of the UB with increasing background wind speed between the simulations is shown in Figure 15b, with the ratio of ensemble-mean lower-PBL background wind speed to the ensemble-mean UB intensity for $U_0 = 0 \text{ m}\cdot\text{s}^{-1}$ as a function of U_0 . Opened circles indicate the cases where the returning lower UB downwind of the UBC center is overcome by background wind (i.e., lower-PBL wind averaged over 5–25 km downwind of the UBC center is directed downwind). In all sensitivity simulations, the returning lower UB is overcome by background wind stronger than ~70% of the UB intensity under the calm condition, consistent with the result from the URBAN simulations. Note that in the SUSHF and SIZE10 simulations, the returning lower UB can be overcome by weaker background wind, compared with the LUSHF, SIZE30, and URBAN simulations, owing to their weaker UB. In all sensitivity simulations, the UBC center is located at the urban center for $U_0 = 0 \text{ m}\cdot\text{s}^{-1}$ and near the downwind boundary of the urban area for $U_0 = 5 \text{ m}\cdot\text{s}^{-1}$, which is consistent with the results of the URBAN simulations (not shown).

Figure 16 shows the distance-time plots of vertical velocity at $z = 400 \text{ m}$ in a single ensemble member for $U_0 = 0 \text{ m}\cdot\text{s}^{-1}$ in the sensitivity simulations. The UB forms near the urban boundaries and advances with time toward the urban center in all sensitivity simulations, as in the URBAN simulations. Meanwhile, UB fronts merge at different times; compared with the URBAN simulations, UB fronts merge ~1.5 hours later in the SUSHF simulations while they merge ~1.5 hours earlier in the LUSHF simulations. This is associated with the smaller (larger) magnitude of urban–rural temperature gradient, which is produced by the smaller (larger) urban surface sensible heat flux in the SUSHF (LUSHF) simulations. In the SIZE10 simulations, the UB fronts merge ~3 hours earlier than in the URBAN simulations, while in the SIZE30 simulations, they merge about 1 hour later. This earlier (later)

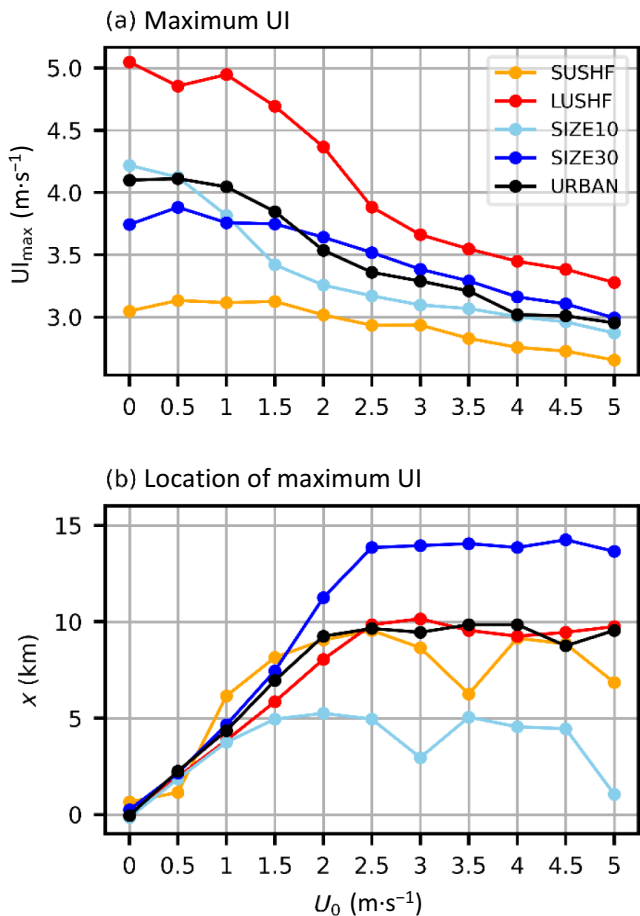
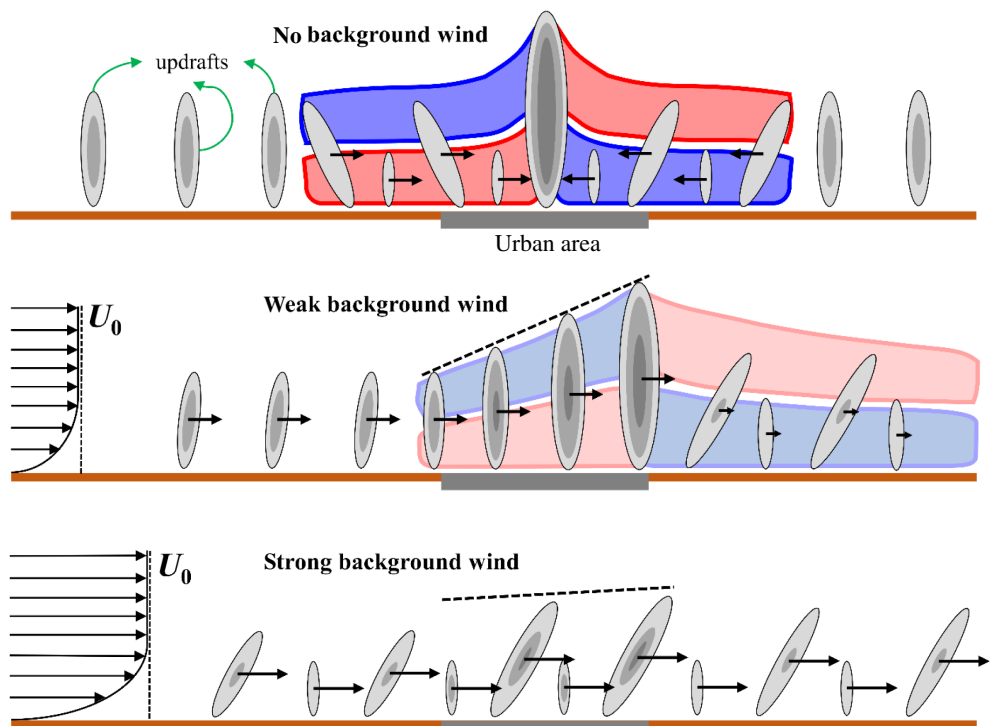


FIGURE 17 (a) Maximum ensemble-mean updraft intensity (UI) and (b) its location as a function of U_0 in the SUSHF, LUSHF, SIZE10, SIZE30, and URBAN simulations. [Colour figure can be viewed at wileyonlinelibrary.com]

merger is mainly attributed to the shorter (longer) distance between the urban boundary and urban center in the SIZE10 (SIZE30) simulations.

Figure 17 shows the maximum ensemble-mean updraft intensity and its location as a function of U_0 in the URBAN, SUSHF, LUSHF, SIZE10, and SIZE30 simulations. All simulations exhibit overall decreasing tendencies of the maximum updraft intensity with increasing U_0 (Figure 17a). The maximum updraft intensity in the LUSHF (SUSHF) simulations is larger (smaller) than that in the URBAN simulations for all U_0 , and the difference between the simulations is relatively large for small U_0 . For $U_0 = 2 \text{ m}\cdot\text{s}^{-1}$, the maximum updraft intensity is $4.4 \text{ m}\cdot\text{s}^{-1}$ in the LUSHF simulations, $3.5 \text{ m}\cdot\text{s}^{-1}$ in the URBAN simulations, and $3.0 \text{ m}\cdot\text{s}^{-1}$ in the SUSHF simulations. While the LUSHF simulations exhibit a sharp decrease in the maximum updraft intensity from $U_0 = 1$ to $2.5 \text{ m}\cdot\text{s}^{-1}$, the SUSHF simulations exhibit relatively very

FIGURE 18 Schematic diagrams that depict the interactions between the UBC and convective cells under no background wind, weak background wind, and strong background wind. The gray shades indicate the magnitude of updraft velocity, and a darker shade means a larger magnitude. The red and blue shades indicate positive and negative anomalies of horizontal wind, respectively, and their lighter colors for weak background wind than for no background wind mean that the anomalies are weaker. Black arrows describe the moving velocities of convective cells. [Colour figure can be viewed at wileyonlinelibrary.com]



small changes with U_0 for the whole U_0 range. The simulations with different sizes of urban area show similar decreasing tendencies of maximum updraft intensity with increasing U_0 . Compared with the URBAN simulations, the SIZE10 simulations exhibit a sharper decrease for small U_0 range, having smaller maximum updraft intensity for $U_0 = 1.5\text{--}3.5 \text{ m}\cdot\text{s}^{-1}$. The SIZE30 simulations show a relatively modest decreasing tendency than the URBAN simulations.

The location of maximum updraft intensity moves downwind as U_0 increases and almost stops moving after it reaches near the downwind boundary of the urban area for all simulations (Figure 17b). This indicates that the appearance of maximum updraft intensity near the urban boundary in the URBAN simulations shown in Figure 5b is not a result of coincidence. Note that four points ($U_0 = 3.5$ and $5 \text{ m}\cdot\text{s}^{-1}$ in the SUSHF simulations and $U_0 = 3$ and $5 \text{ m}\cdot\text{s}^{-1}$ in the SIZE10 simulations) are exceptional, and for all of them, a local maximum of the updraft intensity is located near the urban boundary although it is not the domain maximum. The simulations with different urban surface sensible heat flux show similar tendencies of the location of maximum updraft intensity with increasing U_0 . Because the location of maximum updraft intensity approaches the urban boundary as U_0 increases, it is very sensitive to the size of urban area for large U_0 . The location of maximum updraft intensity in the SIZE10, URBAN, and SIZE30 simulations increases with similar tendencies for small U_0 , but it reaches (near) the urban boundary at $U_0 = 1.5 \text{ m}\cdot\text{s}^{-1}$ in the SIZE10 simulations, at $U_0 = 2 \text{ m}\cdot\text{s}^{-1}$

in the URBAN simulations, and at $U_0 = 2.5 \text{ m}\cdot\text{s}^{-1}$ in the SIZE30 simulations.

4 | SUMMARY AND CONCLUSIONS

In this study, we examined the impacts of background wind on the interactions between the UBC and convective cells through ensemble large-eddy simulations. The analysis results are schematically summarized in Figure 18. For no background wind, a strong updraft forms at the urban center where the UBC center is located and strong vertical wind shear appears in the left and right parts of the UBC. Convective cells in the UBC are advected toward the urban center by the UB, experiencing tilting and weakening. The updrafts of the advected cells merge with the strong updraft at the urban center and enhance it. For weak background wind (e.g., $U_0 = 2.5 \text{ m}\cdot\text{s}^{-1}$), the UBC is displaced downwind and its center is located near the downwind boundary of the urban area. Convective cells intensify and merge with each other while they are passing the urban area, and after they pass the urban boundary, they repeatedly experience tilting and weakening due to the strong vertical wind shear in the downwind area. As a result, the strongest updraft appears near the urban boundary. For strong background wind (e.g., $U_0 = 5 \text{ m}\cdot\text{s}^{-1}$), the UBC is very weak and hardly affects the movement of convective cells. Convective cells are advected mainly by the background wind and repeatedly experience tilting, weakening, and re-intensifying in the urban and rural areas.

Despite the little influence of the UBC, the updrafts of convective cells passing the urban area are stronger than those of convective cells passing the rural area.

The different UBC-convective cell interactions for different background wind speeds lead to the changes in maximum updraft intensity and its location with background wind speed. As the background wind speed increases, the maximum updraft intensity becomes smaller and its location moves downwind until it reaches near the downwind boundary of the urban area. These features are also seen in the sensitivity simulations where the urban surface sensible heat flux and urban size are changed. These imply that urban-induced moist convection is likely to be initiated within cities when background wind is relatively weak and near the downwind boundary of cities, if it is initiated, when background wind is relatively strong.

All simulations in this study are conducted in 2-D settings, which require substantially shorter computation time than 3-D settings and therefore permit a large number of ensemble simulations (total 990 simulations are done in this study). Although the 2-D ensemble simulations enable us to obtain robust insights into the interactions between the UBC and convective cells, the 3-D aspects of UBC and convective cells such as cellular convection and convective rolls cannot be represented in the 2-D simulations. These aspects may be considered in future investigation using 3-D simulations. Previous studies showed that the enhancement of updrafts associated with the interactions between a dryline and convective cells plays an important role in the initiation and development of convective clouds. It would be interesting to examine how the interactions between the UBC and convective cells in the presence/absence of background wind affect the cloud initiation and development in and around urban areas.

ACKNOWLEDGEMENTS

We are grateful to two anonymous reviewers for providing valuable comments on this work. This work was supported by the National Research Foundation of Korea (2021R1A2C1007044).

CONFLICT OF INTEREST STATEMENT

The authors declare no conflict of interest.

DATA AVAILABILITY STATEMENT

The data that support the findings of this study are available from the corresponding author upon reasonable request.

ORCID

Jong-Jin Baik  <https://orcid.org/0000-0003-3709-0532>

REFERENCES

- Atkinson, B.W. & Zhang, J.W. (1996) Mesoscale shallow convection in the atmosphere. *Reviews of Geophysics*, 34, 403–431.
- Avissar, R. & Schmidt, T. (1998) An evaluation of the scale at which ground-surface heat flux patchiness affects the convective boundary layer using large-eddy simulations. *Journal of the Atmospheric Sciences*, 55, 2666–2689.
- Baik, J.-J., Kim, Y.-H. & Chun, H.-Y. (2001) Dry and moist convection forced by an urban heat island. *Journal of Applied Meteorology*, 40, 1462–1475.
- Banghoff, J.R., Sorber, J.D., Stensrud, D.J., Young, G.S. & Kumjian, M.R. (2020) A 10-year warm-season climatology of horizontal convective rolls and cellular convection in central Oklahoma. *Monthly Weather Review*, 148, 21–42.
- Borbora, J. & Das, A.K. (2014) Summertime urban heat island study for Guwahati city, India. *Sustainable Cities and Society*, 11, 61–66.
- Cenedese, A. & Monti, P. (2003) Interaction between an inland urban heat island and a sea-breeze flow: a laboratory study. *Journal of Applied Meteorology*, 42, 1569–1583.
- Chen, G., Zhu, X., Sha, W., Iwasaki, T., Seko, H., Saito, K. et al. (2015) Toward improved forecasts of sea-breeze horizontal convective rolls at super high resolutions. Part II: the impacts of land use and buildings. *Monthly Weather Review*, 143, 1873–1894.
- Christen, A. & Vogt, R. (2004) Energy and radiation balance of a central European city. *International Journal of Climatology*, 24, 1395–1421.
- Cotton, W.R. & Pielke, R.A. (1995) *Human impacts on weather and climate*. Cambridge, UK: Cambridge University Press.
- Dudhia, J. (1989) Numerical study of convection observed during the winter monsoon experiment using a mesoscale two-dimensional model. *Journal of the Atmospheric Sciences*, 46, 3077–3107.
- Falasca, S., Moroni, M. & Cenedese, A. (2013) Laboratory simulations of an urban heat island in a stratified atmospheric boundary layer. *Journal of Visualization*, 16, 39–45.
- Fan, Y., Li, Y., Bejan, A., Wang, Y. & Yang, X. (2017) Horizontal extent of the urban heat dome flow. *Scientific Reports*, 7, 11681.
- Fujibe, F. & Asai, T. (1980) Some features of a surface wind system associated with the Tokyo heat island. *Journal of the Meteorological Society of Japan*, 58, 149–152.
- Ganbat, G., Baik, J.-J. & Ryu, Y.-H. (2015) A numerical study of the interactions of urban breeze circulation with mountain slope winds. *Theoretical and Applied Climatology*, 120, 123–135.
- Han, J.-Y. & Baik, J.-J. (2008) A theoretical and numerical study of urban heat island-induced circulation and convection. *Journal of the Atmospheric Sciences*, 65, 1859–1877.
- Han, J.-Y., Baik, J.-J. & Lee, H. (2014) Urban impacts on precipitation. *Asia-Pacific Journal of Atmospheric Sciences*, 50, 17–30.
- Hidalgo, J., Masson, V. & Pigeon, G. (2008a) Urban-breeze circulation during the CAPITOUL experiment: numerical simulations. *Meteorology and Atmospheric Physics*, 102, 243–262.
- Hidalgo, J., Pigeon, G. & Masson, V. (2008b) Urban-breeze circulation during the CAPITOUL experiment: observational data analysis approach. *Meteorology and Atmospheric Physics*, 102, 223–241.
- Jiang, P., Wen, Z., Sha, W. & Chen, G. (2017) Interaction between turbulent flow and sea breeze front over urban-like coast in large-eddy simulation. *Journal of Geophysical Research: Atmospheres*, 122, 5298–5315.
- Jiménez, P.A., Dudhia, J., González-Rouco, J.F., Navarro, J., Montávez, J.P. & García-Bustamante, E. (2012) A revised scheme for

- the WRF surface layer formulation. *Monthly Weather Review*, 140, 898–918.
- Kang, S.-L. & Lenschow, D.H. (2014) Temporal evolution of low-level winds induced by two-dimensional mesoscale surface heat-flux heterogeneity. *Boundary-Layer Meteorology*, 151, 501–529.
- Khanna, S. & Brasseur, J.G. (1998) Three-dimensional buoyancy- and shear-induced local structure of the atmospheric boundary layer. *Journal of the Atmospheric Sciences*, 55, 710–743.
- Klemp, J.B., Dudhia, J. & Hassiotis, A.D. (2008) An upper gravity-wave absorbing layer for NWP applications. *Monthly Weather Review*, 136, 3987–4004.
- Kniveton, J.C., Bryan, G.H. & Hacker, J.P. (2007) Explicit numerical diffusion in the WRF model. *Monthly Weather Review*, 135, 3808–3824.
- Kropfli, R.A. & Kohn, N.M. (1978) Persistent horizontal rolls in the urban mixed layer as revealed by dual-Doppler radar. *Journal of Applied Meteorology*, 17, 669–676.
- Lee, J.M., Zhang, Y. & Klein, S.A. (2019) The effect of land surface heterogeneity and background wind on shallow cumulus clouds and the transition to deeper convection. *Journal of the Atmospheric Sciences*, 76, 401–419.
- Lee, S.-H. & Baik, J.-J. (2010) Statistical and dynamical characteristics of the urban heat island intensity in Seoul. *Theoretical and Applied Climatology*, 100, 227–237.
- Lemonsu, A. & Masson, V. (2002) Simulation of a summer urban breeze over Paris. *Boundary-Layer Meteorology*, 104, 463–490.
- Lim, K.-S.S. & Hong, S.-Y. (2010) Development of an effective double-moment cloud microphysics scheme with prognostic cloud condensation nuclei (CCN) for weather and climate models. *Monthly Weather Review*, 138, 1587–1612.
- Martilli, A. (2002) Numerical study of urban impact on boundary layer structure: sensitivity to wind speed, urban morphology, and rural soil moisture. *Journal of Applied Meteorology*, 41, 1247–1266.
- Miao, S. & Chen, F. (2008) Formation of horizontal convective rolls in urban areas. *Atmospheric Research*, 89, 298–304.
- Mlawer, E.J., Taubman, S.J., Brown, P.D., Iacono, M.J. & Clough, S.A. (1997) Radiative transfer for inhomogeneous atmospheres: RRTM, a validated correlated-k model for the longwave. *Journal of Geophysical Research*, 102, 16663–16682.
- Moeng, C.-H. & Sullivan, P.P. (1994) A comparison of shear- and buoyancy-driven planetary boundary layer flows. *Journal of the Atmospheric Sciences*, 51, 999–1022.
- Ogawa, S., Sha, W., Iwasaki, T. & Wang, Z. (2003) A numerical study on the interaction of a sea-breeze front with convective cells in the daytime boundary layer. *Journal of the Meteorological Society of Japan*, 81, 635–651.
- Oke, T.R. (1982) The energetic basis of the urban heat island. *Quarterly Journal of the Royal Meteorological Society*, 108, 1–24.
- Oke, T.R., Mills, G., Christen, A. & Voogt, J.A. (2017) *Urban Climates*. Cambridge, UK: Cambridge University Press.
- Omidiar, H., Bou-Zeid, E., Li, Q., Mellado, J.-P. & Klein, P. (2020) Plume or bubble? Mixed-convection flow regimes and city-scale circulations. *Journal of Fluid Mechanics*, 897, A5.
- Peckham, S.E., Williamson, R.B., Wicker, L.J. & Ziegler, C.L. (2004) Numerical simulation of the interaction between the dryline and horizontal convective rolls. *Monthly Weather Review*, 132, 1792–1812.
- Qian, Y., Chakraborty, T.C., Li, J., Li, D., He, C., Sarangi, C. et al. (2022) Urbanization impact on regional climate and extreme weather: current understanding, uncertainties, and future research directions. *Advances in Atmospheric Sciences*, 39, 819–860.
- Ryu, Y.-H., Baik, J.-J. & Han, J.-Y. (2013) Daytime urban breeze circulation and its interaction with convective cells. *Quarterly Journal of the Royal Meteorological Society*, 139, 401–413.
- Ryu, Y.-H., Baik, J.-J. & Lee, S.-H. (2011) A new single-layer urban canopy model for use in mesoscale atmospheric models. *Journal of Applied Meteorology and Climatology*, 50, 1773–1794.
- Salesky, S.T., Chamecki, M. & Bou-Zeid, E. (2017) On the nature of the transition between roll and cellular organization in the convective boundary layer. *Boundary-Layer Meteorology*, 163, 41–68.
- Skamarock, W.C., Klemp, J.B., Dudhia, J., Gill, D.O., Liu, Z., Berner, J. et al. (2019) *A description of the advanced research WRF model version 4*. Colorado, USA: National Center for Atmospheric Research.
- Tewari, M., Chen, F., Wang, W., Dudhia, J., LeMone, M.A., Mitchell, K. et al. (2004) Implementation and verification of the unified Noah land surface model in the WRF model. In: *20th conference on weather analysis and forecasting/16th conference on numerical weather prediction*, 12–15 January 2004. Washington, USA: American Meteorological Society.
- Wang, Q., Hang, J., Fan, Y. & Li, Y. (2020) Urban plume characteristics under various wind speed, heat flux, and stratification conditions. *Atmospheric Environment*, 239, 117774.
- Wang, Q., Wang, Y., Fan, Y., Hang, J. & Li, Y. (2019) Urban heat island circulations of an idealized circular city as affected by background wind speed. *Building and Environment*, 148, 433–447.
- Wang, W. (2009) The influence of thermally-induced mesoscale circulations on turbulence statistics over an idealized urban area under a zero background wind. *Boundary-Layer Meteorology*, 131, 403–423.
- Wang, X. & Li, Y. (2016) Predicting urban heat island circulation using CFD. *Building and Environment*, 99, 82–97.
- Wong, K.K. & Dirks, R.A. (1978) Mesoscale perturbations on airflow in the urban mixing layer. *Journal of Applied Meteorology*, 17, 677–688.
- Xue, M. & Martin, W.J. (2006) A high-resolution modeling study of the 24 May 2002 dryline case during IHOP. Part II: horizontal convective rolls and convective initiation. *Monthly Weather Review*, 134, 172–191.
- Zhang, N., Wang, X. & Peng, Z. (2014) Large-eddy simulation of mesoscale circulations forced by inhomogeneous urban heat island. *Boundary-Layer Meteorology*, 151, 179–194.
- Zhang, Y., Zhang, J., Zhang, X., Zhou, D. & Gu, Z. (2021) Analyzing the characteristics of UHI (urban heat island) in summer daytime based on observations on 50 sites in 11 LCZ (local climate zone) types in Xi'an, China. *Sustainability*, 13, 83.

How to cite this article: Hong, S.H., Jin, H.G. & Baik, J.-J. (2024) Impacts of background wind on the interactions between urban breeze circulation and convective cells: Ensemble large-eddy simulations. *Quarterly Journal of the Royal Meteorological Society*, 150(760), 1518–1537. Available from: <https://doi.org/10.1002/qj.4657>